Shifted boundary polynomial corrections for compressible flows: high order on curved domains using linear meshes

Mirco Ciallella[a,*], Elena Gaburro[a], Marco Lorini[a], Mario Ricchiuto[a]

[a]*Inria, Univ. Bordeaux, CNRS, Bordeaux INP, IMB, UMR 5251, 200 Avenue de la Vieille Tour, 33405 Talence cedex, France*

Abstract

In this work we propose a simple but effective high order polynomial correction allowing to enhance the consistency of all kind of boundary conditions for the Euler equations (Dirichlet, characteristic far-field and slip-wall), both in 2D and 3D, preserving a high order of accuracy without the need of curved meshes. The method proposed is a simplified reformulation of the Shifted Boundary Method (SBM) and relies on a *correction* based on the *extrapolated value* of the in cell polynomial *to the true geometry*, thus not requiring the explicit evaluation of high order Taylor series. Moreover, this strategy could be easily implemented into any already existing finite element and finite volume code. Several validation tests are presented to prove the convergence properties up to order four for 2D and 3D simulations with curved boundaries, as well as an effective extension to flows with shocks.

Keywords: Compressible flows, Curved boundaries, Unstructured linear meshes, Shifted Boundary Method, Discontinuous Galerkin

1. Introduction

The potential of high order methods in providing drastic error reductions in flow simulations with considerable savings in computational costs is well established [66]. A key element in this respect is the proper treatment of *boundary conditions*. This involves two independent aspects: an appropriate geometrical representation of the boundaries and a high order approximation of the boundary condition itself. When dealing with finite elements, the most classical approach is to work with an iso-parametric approximation in which the geometry as well as the flow solution are approximated by some high order polynomial [68]. Standard approaches range from the use of various maps based on some local interpolated or modal polynomial approximation of the curved geometry, to the more recent use of rational B-spline or NURBS approximations used in the so called iso-geometric analysis (IGA) [41]. In both cases, a crucial role is played by the availability of a high quality curved mesh. Progress has been made on methods to obtain such meshes, either via curving straight faced meshes [21, 48, 56, 31, 53, 65], or by using some optimization or variational approach [37, 63, 64]. Despite the advances in this domain, obtaining easily a high quality curved mesh for a complex geometry remains a complex task, still object of intense research both for dominant simplex meshes, and for coarse multiblock quad/hex meshes required in NURBS analysis (cf e.g. [46, 20] and references therein).

In alternative to high order meshing, one can improve the boundary conditions by accounting, on a straight faced mesh, for the local features of the *true* geometry. Early work on curvature corrected wall boundary conditions can be found e.g. in [67], while the specific case of high order schemes and wall boundaries in two space dimensions has been thoroughly treated in the well known paper by Krivodonova and Berger [43]. The last reference in particular proposes an approach to correct the direction used when prescribing the slip-wall condition, which shows a recovery of third and, for some cases, fourth order of accuracy on 2D geometries. However, this method can be formulated only for slip-wall conditions, and the work is limited to 2D geometries.

*Corresponding author

Email addresses: mirco.ciallella@inria.fr (Mirco Ciallella), elena.gaburro@inria.fr (Elena Gaburro), marco.lorini@inria.fr (Marco Lorini), mario.ricchiuto@inria.fr (Mario Ricchiuto)

More recent developments addressing this problem can be found in [18, 19, 30]. The authors first presented a reconstruction off-site data (ROD) approach, in a high order finite volume framework, to apply Dirichlet boundary conditions [18]. Afterwards, the work has also been extended to other boundary conditions [19], which represents an important improvement for real applications. Due to the finite volume framework, the approach is built on the least-squares method, which is used to handle several constraints from scattered mean values associated to the elements. Due to the linear system arising from the constrained least-squares problem, a matrix should be inverted locally and this may introduce some issues for ill-conditioned problems.

In this work, we propose an alternative path to achieve a similar result. Our idea relies on a simplified reformulation of the Shifted Boundary Method (SBM) [49, 50, 57, 54, 45, 14, 1, 17] that enhances the consistency of all kinds of boundary conditions for the Euler equations (Dirichlet, characteristic far-field and slip-wall), both in 2D and 3D. Originally, SBM has been introduced to cope with embedded boundary problems and it consists in retaining the designed order of accuracy of the discretization method by using modified boundary conditions based on truncated Taylor series expansions. Here we propose a *simplified version* which allows to avoid the cumbersome explicit evaluation of all the Taylor development terms [54, 2], and directly exploits the available (nodal or modal) polynomial expansion of a physical, linear element. The approach has been easily implemented for steady problems using indifferently nodal and modal bases on simplex meshes, and its extension to time dependent problems is based on the ADER space-time formulation. The ADER methodology has been introduced by Toro and collaborators in [60, 61, 62] and it has been substantially simplified and generalized in [24]. Then, the ADER approach has been widely used in the last 15 years: we recall here only some of its main developments, as the extension to staggered meshes [58, 59] to unstructured 2D and 3D moving meshes [47, 9, 34, 33], to semi-implicit and implicit schemes [52, 10, 40], its coupling with the MOOD *a posteriori* finite volume limiter [7, 35] and its application in the modeling of quite complex PDE systems, as MHD in [3, 29], GRMHD and CCZ4 in [28, 26, 25] and multiphase models and the recent first order hyperbolic unified model for continuum mechanics, known as GPR system, in [55, 13, 32, 6]. Although the extensive use of ADER schemes, the problems related to high accurate treatment of boundary conditions have been only marginally considered, see for example the work [42] that however treats the topic from a completely different approach employing indeed a diffuse interface technique. Finally, for a formulation of ADER schemes employing a genuinely space-time *modal expansion*, as the one adopted in this work, we refer to [34, 36].

The paper is organized as follows. First, in Section 2 we describe the physical model of interest in this work, represented by the Euler equations of gasdynamic on curved domains. Due to the generality of the approach, it should be noticed that the method proposed here can be easily applied to other systems of equations [49, 50]. Next, in Section 3 we briefly recall the general framework of Discontinous Galerkin (DG) schemes, used here to discretize the governing PDEs system with high order of accuracy in space and time on conformal meshes; in particular, a brief overview on the standard treatment of boundary conditions, involving the necessity of using curved meshes for curved domain, is given in Section 3.5. Then, the core of the paper is represented by Section 4, where we present the *polynomial correction* to be applied to general high order numerical schemes directly on *linear* fitted meshes for modeling *compressible* flows on *curved* domains. We would like to remark that the presented approach is simple, independent on the underlying type of high order discretization and on the space dimension and allows to retrieve the formal order of accuracy of the original method for arbitrary domain and obstacles shapes. Finally, a large set of numerical simulations, allowing to validate the proposed polynomial correction, is presented in Section 5, for both far-field and slip-wall boundary conditions, steady and unsteady problems, on two and three dimensional curved domains. The paper is closed by some conclusive remarks and an outlook to future works is given in Section 6.

2. Governing equations

We consider the numerical approximation of solutions of the Euler equations in d space dimensions reading:

$$\partial_t \mathbf{U} + \nabla \cdot \mathbf{F}(\mathbf{U}) = 0, \quad \text{on} \quad \Omega_T = \Omega \times [0, T] \subset \mathbb{R}^d \times \mathbb{R}^+, \tag{1}$$

with $\mathbf{U}$ the vector of conserved variables and $\mathbf{F}$ the non linear flux respectively defined as

$$\mathbf{U} = \begin{pmatrix} \rho \\ \rho\mathbf{u} \\ \rho E \end{pmatrix}, \quad \mathbf{F} = \begin{pmatrix} \rho\mathbf{u} \\ \rho\mathbf{u}\otimes\mathbf{u} + p\mathbb{I} \\ \rho H\mathbf{u} \end{pmatrix}, \tag{2}$$

having denoted by ρ the mass density, by $\mathbf{u}$ the velocity, by p the pressure, and with $E = e + \mathbf{u}\cdot\mathbf{u}/2$ the specific total energy, e being the specific internal energy. Finally, the total specific enthalpy is $H = h + \mathbf{u}\cdot\mathbf{u}/2$ with $h = e + p/\rho$ the specific enthalpy. For simplicity in this paper we work with the classical perfect gas equation of state

$$p = (\gamma - 1)\rho e, \tag{3}$$

with γ the constant ratio of specific heats.

In order to perform convergence analysis, we use the manufactured solution method which needs the discretization of an additional source term in Equation (1) which thus reads as follow

$$\partial_t \mathbf{U} + \nabla\cdot\mathbf{F}(\mathbf{U}) = \mathbf{S}(\mathbf{U}). \tag{4}$$

For this reason we are going to include $\mathbf{S}$ in the discretization presented in Section 3.

3. High order Discontinuous Galerkin discretization

3.1. Computational domain and data representation

The spatial domain Ω is discretized by means of a tessellation $\mathscr{T}$ composed of $\mathscr{N}$ non-overlapping simplicial elements (triangles in 2D, tetrahedra in 3D). We denote by K the generic element, so that $\Omega_h = \bigcup_{j=1}^{\mathscr{N}} K_j$. Note that in general $\Omega_h \neq \Omega$ and in particular $\partial\Omega_h \neq \partial\Omega$ for most approximations, even conformal, with the exception of very simple geometries or of iso-geometric approaches [41].

The numerical solution $\mathbf{U}$ is approximated by $\mathbf{U}_h$, which belongs to a space of piece-wise polynomials within each triangle K and discontinuous across faces, such that in each element K_j we have

$$\mathbf{U}_h(\mathbf{x},t)|_{K_j} = \sum_{i=1}^{D} \mathbf{U}_k(t)\psi_k(\mathbf{x}), \tag{5}$$

where $\{\psi_k, k = 1,\dots,D\}$ is a basis of polynomials of degree p. On simplex elements, the number of *degrees of freedom* D can be shown to be $D = \prod_{l=1}^{d}(p+l)/l$. The discontinuous finite element data representation (5) leads to a Finite Volume (FV) scheme if $p = 0$.

3.2. Discontinuous Galerkin discretization in space

The elemental semi-discrete discontinuous Galerkin (DG) weak formulation is classically written by projecting each component of (4) on the relevant basis and integrating by parts [16, 5].

$$\int_K \psi_i \frac{\mathrm{d}\mathbf{U}_h}{\mathrm{d}t}\mathrm{d}\mathbf{x} + \int_{\partial K} \psi_i \hat{F}(\mathbf{U}_h^-, \mathbf{U}_h^+)\cdot\mathbf{n}\mathrm{d}S - \int_K \nabla\psi_i \cdot \mathbf{F}(\mathbf{U}_h)\mathrm{d}\mathbf{x} = \int_K \psi_i \mathbf{S}(\mathbf{U}_h)\mathrm{d}\mathbf{x}, \qquad 1 \le i \le D, \tag{6}$$

with $\hat{F}(\mathbf{U}_h^-, \mathbf{U}_h^+)$ a consistent numerical flux which depends on the face values of the internal state $\mathbf{U}_h^-$, of the neighboring element state $\mathbf{U}_h^+$ and on the face normal $\mathbf{n}$. We recall in particular that a consistent flux is a Lipschitz continuous function of each of its arguments which also veryfies

$$\hat{F}(\mathbf{u},\mathbf{u})\cdot\mathbf{n} = \mathbf{F}(\mathbf{u})\cdot\mathbf{n} \tag{7}$$

In this work we have used a simple and robust Rusanov-type flux:

$$\hat{F}(\mathbf{U}_h^-, \mathbf{U}_h^+)\cdot\mathbf{n} = \frac{1}{2}\left(\mathbf{F}(\mathbf{U}_h^+) + \mathbf{F}(\mathbf{U}_h^-)\right)\cdot\mathbf{n} - \frac{1}{2}s_{max}\left(\mathbf{U}_h^+ - \mathbf{U}_h^-\right), \tag{8}$$

where s_{max} is the maximum eigenvalue of the Jacobians of the flux $A_{\mathbf{n}}\left(\mathbf{U}_h^+\right)$ and $A_{\mathbf{n}}\left(\mathbf{U}_h^-\right)$.

3.3. High order time integration

In this Section we briefly recall two classical different strategies, both employed in this work, to achieve high order of accuracy during the time integration with a discontinous Galerkin scheme.

3.3.1. Method of lines for steady problems

For steady state computations, we use a classical method of lines. Assembling all the contributions (6), we obtain in each element K a system of ODEs [5] reading

$$\frac{\mathrm{d}\mathbf{U}}{\mathrm{d}t} + M^{-1}\mathsf{R}(\mathbf{U}) = 0, \tag{9}$$

where the array $\mathbf{U}$ contains the $d+2$ vector of unknowns corresponding to the degrees of freedom, R is the array of size D, made up by the second, third, and fourth integrals in (6), and M denotes the elemental mass matrix with $D \times D$ block diagonal entries, whose components are given by

$$[M]_{ik} = \int_K \psi_i \psi_k \mathrm{d}\mathbf{x}\,. \tag{10}$$

For steady problems, we simply integrate (9) with explicit Euler or classical Runge-Kutta methods with improved time step constraints [11, 39].

3.3.2. High order explicit ADER approximation with local space-time predictors

For time accurate simulations, we have used a high order explicit one-step *predictor-corrector* ADER approach, that we are going to briefly describe in this section. For further details we refer to [24, 34]. The temporal domain is as usual discretized in temporal slabs $[t^n, t^{n+1}]$. With the same notation used before, on fixed meshes the ADER method can be succinctly written as

$$\mathbf{U}^{n+1} = \mathbf{U}^n - M^{-1} \int_{t^n}^{t^{n+1}} \mathsf{R}(\mathbf{q}_h) dt, \tag{11}$$

where $\mathbf{q}_h = \mathbf{q}_h(\mathbf{x}, t)$ is a high order space-time predictor of the solution in the time slab $[t^n, t^{n+1}]$. In practice, (11) is replaced by some high order quadrature formula in time (with α_i and ω_i, $1 \le i \le r$, the quadrature points and weights)

$$\mathbf{U}^{n+1} = \mathbf{U}^n - M^{-1}\Delta t \sum_{i=1}^{r} \omega_i \mathsf{R}(\mathbf{q}_h(t^{n+\alpha_i})), \tag{12}$$

and $\mathbf{q}_h(\mathbf{x}, t)$ is defined as a polynomial of degree N in space *and* time, with $N \ge p$. This polynomial is obtained by means of a genuinely local space-time procedure. In the current implementation this local problem is formulated by means of a modal expansion

$$\mathbf{q}_h(\mathbf{x}, t) = \sum_{\ell=0}^{Q-1} \theta_\ell(\mathbf{x}, t)\mathbf{q}_\ell^n, \qquad (\mathbf{x}, t) \in K \times [t^n, t^{n+1}], \qquad Q = \mathcal{L}(N, d+1), \tag{13}$$

where $\theta_\ell(\mathbf{x}, t)$ being $\mathcal{L}(N, d) = \prod_{m=1}^{d}(N+m)/m$ space-time modal basis of the polynomials of degree N in $d+1$ dimensions (d space dimensions and time), defined as

$$\theta_\ell(x, y, t)|_{K\times[t^n,t^{n+1}]} = \frac{(x - x_K^n)^{p_\ell}}{p_\ell! h_K{}^{p_\ell}} \frac{(y - y_K^n)^{q_\ell}}{q_\ell! h_K^{q_\ell}} \frac{(t - t^n)^{r_\ell}}{r_\ell! h_K^{r_\ell}}, \quad \ell = 0, \ldots, \mathcal{L}(N, d+1), \quad 0 \le p_\ell + q_\ell + r_\ell \le N, \tag{14}$$

with (x_K, y_K) the gravity center of element K, and (p_ℓ, q_ℓ, r_ℓ) being the terms associated to the taylor series expansion. The values of the predictor $\mathbf{q}_h^n$ are computed by means of an iterative procedure that seeks the solution for any space-time element $K \times [t^n, t^{n+1}]$ of the local space-time weak formulation

$$\begin{aligned}
&\int_K \theta_k(\mathbf{x}, t^{n+1})\mathbf{q}_h^n(\mathbf{x}, t^{n+1})\mathrm{d}\mathbf{x} - \int_K \theta_k(\mathbf{x}, t^n)\mathbf{U}_h^n(\mathbf{x}, t^n)\mathrm{d}\mathbf{x} - \\
&\int_{t^n}^{t^{n+1}} \int_K \frac{\partial \theta_k}{\partial t}(\mathbf{x}, t)\mathbf{q}_h^n(\mathbf{x}, t)\mathrm{d}\mathbf{x}\mathrm{d}t + \int_{t^n}^{t^{n+1}} \int_K \theta_k(\mathbf{x}, t)\nabla \cdot \mathbf{F}(\mathbf{q}_h^n)\mathrm{d}\mathbf{x}\mathrm{d}t = \int_{t^n}^{t^{n+1}} \int_K \theta_k(\mathbf{x}, t)\,\mathbf{S}(\mathbf{q}_h^n)\mathrm{d}\mathbf{x}\mathrm{d}t,
\end{aligned} \tag{15}$$

where $\mathbf{U}_h^n$ is the known initial condition at time t^n.

Equation (15) is fully local, in the sense that it involves no communication between K and its neighbouring control volumes. The solution to this equation can be obtained *independently within each element K* by means of some iterative procedure. In this work a simple discrete Picard iteration for each space-time element is used.

3.4. A posteriori sub-cell finite volume limiter and CFL constraint

To handle discontinuous solutions in the time dependent case we use the MOOD approach [15, 22, 23], which has already been effectively applied in the ADER framework [47, 8, 35].

The algorithm is based on an *a posteriori* technique. The solution is first evolved from t^n to t^{n+1} using the high order ADER-DG method. Then several admissibility criteria are checked and the solution in all troubled cells (i.e. the cells not satisfying the admissibility criteria) is recomputed *a posteriori* using a MUSCL-Hancock TVD finite volume (FV) scheme, but working on a sub-triangulation of the initial grid in order to preserve the accuracy of the high order DG scheme also when passing to a lower order but more robust second order FV scheme. All aspects of the implementation of this technique are provided in [35] to which we refer for details.

Concerning the choice of the time step, we have implemented the usual explicit CFL condition

$$\Delta t < CFL\left(\frac{|h_{\min}|}{(2N+1)|\lambda_{\max}|}\right), \tag{16}$$

where $|h_{min}|$ is the minimum characteristic mesh-size and $|\lambda_{max}|$ is the maximum eigenvalue of the Jacobian of the flux. For DG on unstructured meshes the CFL stability condition requires the inequality $CFL < 1/d$ to be satisfied (cf. discussion in [12]). We underline that the time step constraint does not need to be modified in presence of troubled cells, because we subdivide each troubled triangle in exactly $(2N+1)^d$ sub-triangles and then we employ a FV scheme for which (16) holds with $N = 0$. We refer again to [35] for details.

3.5. Boundary conditions on conformal meshes

When the boundary ∂K of element K belongs to $\partial\Omega_h$, the normal flux function $\mathbf{F}(\mathbf{U}_h)\cdot\mathbf{n}$ must account for the appropriate boundary conditions. The flux consistent with such conditions will be denoted by $\mathbf{F}_{\mathbf{n}}^{bc}$. In this work, the boundary flux function $\mathbf{F}_{\mathbf{n}}^{bc}$ is obtained by defining a ghost state $\mathbf{U}^{bc}$, and introducing a numerical flux $\mathbf{F}_{\mathbf{n}}^{bc} = \hat{F}(\mathbf{U}_h^-, \mathbf{U}^{bc})$ defined by some approximate Riemann solver based on the internal state $\mathbf{U}_h^-$ and on $\mathbf{U}^{bc}$. Depending on the condition to be enforced, different definitions of the ghost state are used:

- for far-field, which can be seen as a Dirichlet-type BC enforced weakly through fluxes, all the components of $\mathbf{U}^{bc}$ are set to prescribed values;
- at inflow/outflow boundaries $\mathbf{U}^{bc}$ is obtained by imposing the Riemann invariants associated to characteristics entering the domain values obtained from prescribed reference values of density, pressure and Mach number;
- for slip walls we wish to set

$$\mathbf{u}\cdot\mathbf{n} = w. \tag{17}$$

  In this case $\mathbf{U}^{bc}$ has the same density, internal energy and tangential velocity of $\mathbf{U}_h^-$, and the opposite normal relative velocity component $\mathbf{u}\cdot\mathbf{n} - w$. For this condition, an alternative way consists in defining directly the boundary flux function by setting $\mathbf{u}\cdot\mathbf{n} = w$, meaning that

$$\mathbf{F}_{\mathbf{n}}^{bc} = \mathbf{F}_{\mathbf{n}}(\mathbf{U}^{bc}) = (\rho w,\ \rho\mathbf{u}\, w + p\,\mathbf{n},\ \rho H\, w)\ . \tag{18}$$

  When doing so, the value of the total enthalpy should be consistently modified as

$$H = \frac{\gamma}{\gamma-1}\frac{p}{\rho} + \frac{1}{2}\left(w^2 + u_{\mathbf{t}}^2\right), \tag{19}$$

  with $u_{\mathbf{t}} = \mathbf{u}\cdot\mathbf{t}$ the tangent velocity. For static walls this reduces to $w = 0$ and $\mathbf{F}_{\mathbf{n}}^{bc} = (0,\ p\,\mathbf{n},\ 0)$.

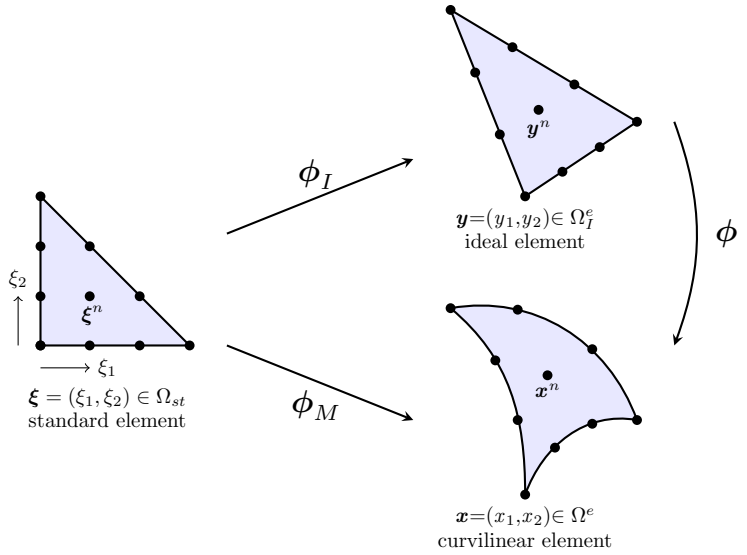

Figure 1: We give here a visual idea of the necessary transformations to be employed when dealing with curved meshes. First, one needs the map from a standard reference element Ω_{st} (left) onto the straight-sided element Ω_I^e (top right), i.e. the mapping $\boldsymbol{\phi}_I : \Omega_{st} \to \Omega_I^e$, and the one onto the curvilinear element (bottom right), i.e. $\boldsymbol{\phi}_M : \Omega_{st} \to \Omega^e$. Finally, the deformation mapping $\boldsymbol{\phi} : \Omega_I^e \to \Omega^e$ is defined through the composition $\boldsymbol{\phi} = \boldsymbol{\phi}_M \circ \boldsymbol{\phi}_I^{-1}$.

For high order methods, one of the key aspects in order to achieve a genuinely high order of accuracy is represented by the ability of simultaneously control the error on the geometry and the flow variables. This also includes approximating boundary integrals using consistent quadrature rules. To this end, an obvious, but also complex and expensive, solution consists in the use of a curved high order approximation of the boundary of the domain, which usually entails the use of some iso-parametric approximation of the boundary and the generation of a valid curved volume mesh [66]. Curvilinear grids represent geometric boundaries with far superior accuracy allowing the use of larger elements than would be possible with linear elements. Several approaches exist to obtain valid high order meshes, either based on curving existing linear meshes [21, 48, 56, 31, 53], or on some optimization or variational method [37, 63, 64]. Moreover, these approaches always require the definition and evaluation of mappings between the curvilinear elements and the reference elements (see Figure 1), and despite the recent progress, while the generation of linear meshes for complex geometries has reached a very high level of maturity, the robust generation of curved meshes remains a relatively complex issue.

In this work we employ linear and curved meshes generated by the open source mesh generator `Gmsh` [38], and in the next Section, which represents the core of this work, we will show a novel technique to retrieve high order of accuracy for curved domain using linear meshes.

4. High order boundary conditions on linear meshes via polynomial corrections

In this work we aim at side stepping the need of generating curved meshes allowing to use directly conformal linear ones. The idea is to use a simplified formulation of the Shifted Boundary Method (SBM), originally introduced to handle non-conformal meshes within second order of accuracy for elliptic, parabolic and hyperbolic problems [49, 50, 57], in order to compensate geometrical errors and retain the desired high order of accuracy.

For the sake of clarity, we recall briefly the notation employed at boundaries. Let Ω_h be a *linear* conformal mesh discretizing the physical domain Ω, and $\tilde{\Gamma} := \partial\Omega_h$ the *linear* approximation of the curved boundary $\Gamma = \partial\Omega$. In particular, we refer to $\tilde{\Gamma}$ as to the *surrogate boundary*. Moreover, for any point on $\tilde{\Gamma}$ we assume to be able to define a

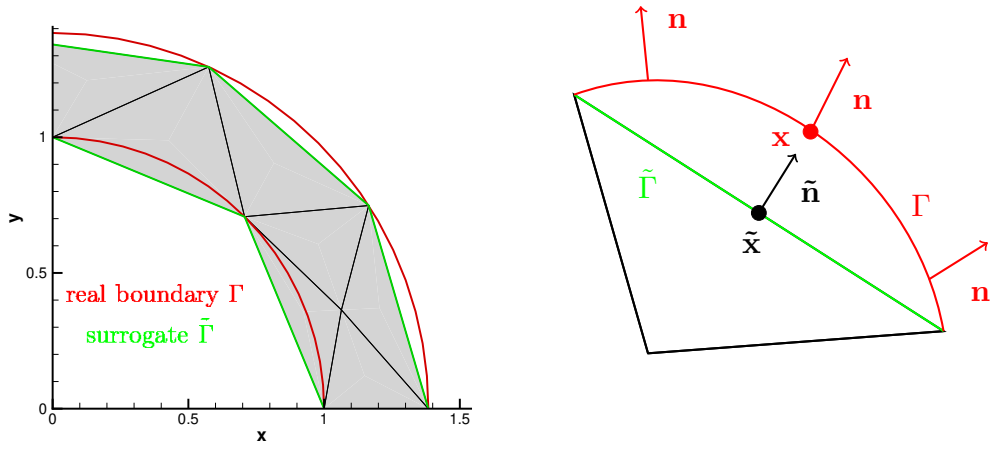

Figure 2: The SBM: the surrogate and actual boundaries with correspondent normals.

map to a unique point on the *true boundary* Γ, s.t.

$$\begin{aligned} \mathcal{R} : \tilde{\Gamma} &\to \Gamma \\ \tilde{\mathbf{x}} &\to \mathbf{x}. \end{aligned}$$

The map $\mathcal{R}$ can be built in several ways, for example using a closest point projection, or using level sets, or equivalently using distances along directions normal to the true boundary Γ, as shown in Figure 2. Since the gap between $\tilde{\Gamma}$ and Γ is going to be of crucial importance, in terms of accuracy of the solution, the map $\mathcal{R}$ will be characterized by a distance vector function:

$$\mathbf{d}(\tilde{\mathbf{x}}) \;=\; \mathbf{x} \,-\, \tilde{\mathbf{x}} \;=\; [\mathcal{R} - \mathbf{I}](\tilde{\mathbf{x}}). \tag{20}$$

In our case, $\mathcal{R}$ is built using distances along normals to Γ, the vector $\mathbf{d}(\tilde{\mathbf{x}})$ is parallel to $\mathbf{n}(\mathbf{x})$ (the vector normal to Γ in $\mathbf{x} = \mathcal{R}(\tilde{\mathbf{x}})$) such that

$$\mathbf{x} = \tilde{\mathbf{x}} + \mathbf{d}(\tilde{\mathbf{x}}), \quad \mathbf{d}(\tilde{\mathbf{x}}) = \mathbf{n}(\mathbf{x})\|\mathbf{d}(\tilde{\mathbf{x}})\|.$$

Following the shifted boundary approach, we now modify the boundary conditions to retain the appropriate consistency order. We give a detailed description of the basic method for *Dirichlet* conditions. Let ρ_D be the prescribed value of the density (similar expressions can be written for all variables). The main idea is that a smooth exact solution of the problem will verify the estimate

$$\begin{aligned} \rho_D(\tilde{\mathbf{x}} + \mathbf{d}) = \rho(\tilde{\mathbf{x}}) + \|\mathbf{d}\| \sum_{j=1}^{d} n_j \, \partial_{x_j}\rho(\tilde{\mathbf{x}}) + \|\mathbf{d}\|^2 \sum_{j=1}^{d}\sum_{k=1}^{d} \frac{1}{2!} \, n_j n_k \, \partial^2_{x_j x_k}\rho(\tilde{\mathbf{x}}) \\ + \|\mathbf{d}\|^3 \sum_{j=1}^{d}\sum_{k=1}^{d}\sum_{\ell=1}^{d} \frac{1}{3!} \, n_j n_k n_\ell \, \partial^3_{x_j x_k x_\ell}\rho(\tilde{\mathbf{x}}) + \dots \quad . \end{aligned} \tag{21}$$

The idea is thus to modify the boundary condition on $\tilde{\Gamma}$ to account for all the corrective terms, which boils down to

use a modified prescribed value ρ_{SBM} which, for different accuracy orders, is given by

$$\begin{aligned}
\rho_{\text{SBM}}(\tilde{\mathbf{x}}) = \rho_D(\tilde{\mathbf{x}} + \mathbf{d}) &- \|\mathbf{d}\| \sum_{j=1}^{d} n_j \, \partial_{x_j} \rho(\tilde{\mathbf{x}}) && \text{second order} \\
&- \|\mathbf{d}\|^2 \sum_{j=1}^{d} \sum_{k=1}^{d} \frac{1}{2!} \, n_j n_k \, \partial^2_{x_j x_k} \rho(\tilde{\mathbf{x}}) && \text{third order} \\
&- \|\mathbf{d}\|^3 \sum_{j=1}^{d} \sum_{k=1}^{d} \sum_{\ell=1}^{d} \frac{1}{3!} \, n_j n_k n_\ell \, \partial^3_{x_j x_k x_\ell} \rho(\tilde{\mathbf{x}}) && \text{fourth order} \\
&\dots \, .
\end{aligned} \tag{22}$$

Note that for an explicit method all the terms involved in the right hand side of the last expression are known. For implicit schemes, they will modify the structure of the algebraic equations obtained. Also note that all the derivative terms are evaluated starting from the available finite element approximation, and sampled at the appropriate quadrature points. Please refer to [2, 54] for more details.

4.1. Derivative free formulation via polynomial corrections

The correction terms in (22) become more and more cumbersome and costly as the order of accuracy is increased, especially in three space dimensions. We propose here a different formulation that somehow *simplifies* the evaluation of these terms, especially on straight-sided simplicial meshes for which both nodal and modal bases can be easily evaluated in physical space, without the needing of a map to the reference space, which would be instead required for curved elements.

Starting from a Taylor series expansion of arbitrary order of accuracy, for a generic variable P, centered in $\tilde{\mathbf{x}}$

$$P(\tilde{\mathbf{x}} + \mathbf{d}) = P(\tilde{\mathbf{x}}) + \nabla P(\tilde{\mathbf{x}}) \cdot \mathbf{d} + \frac{1}{2} \mathbf{d}^{\intercal} \cdot \mathscr{H}(P(\tilde{\mathbf{x}})) \cdot \mathbf{d} + \dots \quad ,$$

and moving $P(\tilde{\mathbf{x}})$ in the left-hand-side of the equation, we are left with

$$P(\tilde{\mathbf{x}} + \mathbf{d}) - P(\tilde{\mathbf{x}}) = \nabla P(\tilde{\mathbf{x}}) \cdot \mathbf{d} + \frac{1}{2} \mathbf{d}^{\intercal} \cdot \mathscr{H}(P(\tilde{\mathbf{x}})) \cdot \mathbf{d} + \dots \quad .$$

Therefore, by simply evaluating the polynomial P in $\tilde{\mathbf{x}} + \mathbf{d}$ and by calculating the difference with that evaluated in $\tilde{\mathbf{x}}$ we get all the necessary correction terms in *only one* polynomial evaluation. A more interesting way to see our approach is to realize that the Taylor series expansion truncated to the same degree as the underlying elemental polynomial corresponds to a change of basis for the finite element space, passing to the local point wise Taylor basis. In this respect, the original SBM uses a different basis in different quadrature points, which is expensive and unnecessary.

In practice, the data required in all quadrature points can be evaluated using the unique basis available in the implementation, whatever that may be. Note also that the use of linear meshes, makes the finite element mapping fully linear, thus passing from the reference to the physical space can be done with no ambiguity for any type of basis, and for all degrees of approxmation.

For example, in practice the modified Dirichlet condition for the density ρ, introduced in (22), can be rewritten as

$$\rho_{\text{SBM}}(\tilde{\mathbf{x}}) = \rho_D(\tilde{\mathbf{x}} + \mathbf{d}) - \left[\rho(\tilde{\mathbf{x}} + \mathbf{d}) - \rho(\tilde{\mathbf{x}})\right] = \rho(\tilde{\mathbf{x}}) + \left[\rho_D(\tilde{\mathbf{x}} + \mathbf{d}) - \rho(\tilde{\mathbf{x}} + \mathbf{d})\right], \tag{23}$$

which shows that the correction of the SBM method can be also seen as a direct *shift* on the surrogate boundary of the extrapolated polynomial error on the true boundary.

This much simpler formulation only requires one extra polynomial evaluation and thus it can be readily implemented on straight sides simplex elements for which the basis functions are easily expressed in the physical space. As we mentioned above, these extrapolated variables are then used to compose a *ghost state* $\mathbf{U}^{bc}$ that will be used, along with the internal state $\mathbf{U}_h^-$, as input for the numerical flux $\hat{F}(\mathbf{U}_h^-, \mathbf{U}^{bc})$ to obtain the consistent boundary flux $\mathbf{F}_{\mathbf{n}}^{bc}$.

4.2. Treatment of slip wall boundary conditions

A similar approach can be applied in order to impose the slip wall boundary condition (17) on the surrogate boundary $\tilde{\mathbf{x}}$. An important issue to take into account in this case is that, besides the position of the surrogate wall boundary $\tilde{\Gamma}_w$, also its normal $\tilde{\mathbf{n}}$ does not coincide with $\mathbf{n}$, the normal to the true wall boundary Γ_w. This difference affects both the magnitude and the rate of the convergence of the error as shown e.g. in [43, 5, 4]. To overcome this issue, here we start from the formulation used in [57]. We start by decomposing the unit normal vector $\tilde{\mathbf{n}}$ at $\tilde{\mathbf{x}}$ as

$$\tilde{\mathbf{n}} = (\tilde{\mathbf{n}} \cdot \mathbf{n})\,\mathbf{n} + \sum_{k=1}^{d-1} (\tilde{\mathbf{n}} \cdot \mathbf{t}_k)\,\mathbf{t}_k,$$

where $\mathbf{t}_k$ are the vector tangent to Γ_w. By doing so, $\mathbf{F}^{bc}_{\tilde{\mathbf{n}}}$ can be recast as

$$\mathbf{F}^{bc}_{\tilde{\mathbf{n}}} = (\tilde{\mathbf{n}} \cdot \mathbf{n})\mathbf{F}_{\mathbf{n}} + \sum_{k=1}^{d-1} (\tilde{\mathbf{n}} \cdot \mathbf{t}_k)\mathbf{F}_{\mathbf{t}_k}. \tag{24}$$

Then we can apply the Taylor expansion to the normal velocity appearing in the flux terms, while the other terms like ρ and p are taken from $\tilde{\mathbf{x}}$ without any corrections,

$$\mathbf{F}_{\mathbf{n}} = \begin{pmatrix} \rho w_{\text{SBM}} \\ \rho w_{\text{SBM}}\,\mathbf{u} + p\,\mathbf{n} \\ \rho w_{\text{SBM}}\,H \end{pmatrix}, \qquad \mathbf{F}_{\mathbf{t}_k} = \begin{pmatrix} \rho\, u_{\mathbf{t}_k} \\ \rho\, u_{\mathbf{t}_k}\,\mathbf{u} + p\,\mathbf{t}_k \\ \rho\, u_{\mathbf{t}_k}\,H \end{pmatrix}, \tag{25}$$

such that,

$$\begin{aligned} w_{\text{SBM}} = w &- \|\mathbf{d}\| \sum_{i=1}^{d} n_i \sum_{j=1}^{d} n_j\, \partial_{x_j} u_i(\tilde{\mathbf{x}}) && \text{second order} \\ &- \|\mathbf{d}\|^2 \sum_{i=1}^{d} n_i \sum_{j=1}^{d} \sum_{k=1}^{d} \frac{1}{2!}\, n_j n_k\, \partial^2_{x_j x_k} u_i(\tilde{\mathbf{x}}) && \text{third order} \\ &- \|\mathbf{d}\|^3 \sum_{i=1}^{d} n_i \sum_{j=1}^{d} \sum_{k=1}^{d} \sum_{\ell=1}^{d} \frac{1}{3!}\, n_j n_k n_\ell\, \partial^3_{x_j x_k x_\ell} u_i(\tilde{\mathbf{x}}) && \text{fourth order} \\ &\dots , \end{aligned} \tag{26}$$

having set $\mathbf{n} = \{n_j\}_{j=1,\dots,d}$ and $\mathbf{u} = \{u_j\}_{j=1,\dots,d}$.

As done before, we use the fact that the Taylor series development on the right hand side of (26) is exact when applied to a polynomial of degree lower or equal to the employed expansion, and thus we simplify it and we recast the correction as

$$w_{\text{SBM}} = \mathbf{u}(\tilde{\mathbf{x}}) \cdot \mathbf{n} + [w - \mathbf{u}(\tilde{\mathbf{x}} + \mathbf{d}) \cdot \mathbf{n}]\,. \tag{27}$$

It should be noticed that, without the formulation in Eq. (27), in order to perform the extrapolation given in Eq. (26), high order derivatives of the velocity components would have been needed. However, since all derivatives are usually computed with respect to the conserved variables, either the *chain rule* or some kind of linearization would have been to be implemented to recover the necessary higher order derivatives.

Remark 1 (Boundary flux and penalty term). *When using the numerical flux* (18) *instead of a classical numerical flux* $\hat{F}(\mathbf{U}_h^-, \mathbf{U}^{bc}_{\tilde{\Gamma}})$ *(as the Rusanov flux), for high (third, fourth, etc) order schemes, in order to obtain the correct convergence rates we had to include a penalty term similar to the diffusion term of the Rusanov flux. For slip walls this term reads*

$$\mathcal{P}_w := \alpha_w \left(\mathbf{U} - \mathbf{U}^{bc}_{\tilde{\Gamma}}\right) = \alpha_w \rho \begin{pmatrix} 0 \\ \mathbf{u} \cdot \mathbf{n} - w_{SBM} \\ \dfrac{(\mathbf{u} \cdot \mathbf{n})^2}{2} - \dfrac{w_{SBM}^2}{2} \end{pmatrix}, \tag{28}$$

where $\alpha_w = \|\mathbf{u}\| + \sqrt{\gamma p/\rho}$.

Finally, for non moving walls with $w = 0$ we consider the simpler strategy consisting in imposing directly $W := (\rho\mathbf{u}\cdot\mathbf{n})|_{\Gamma_w} = 0$. This allows to work with derivatives and variations of the momentum variable. We thus replace (26) by

$$\begin{aligned} W_{SBM} = &- \|\mathbf{d}\| \sum_{i=1}^{d} n_i \sum_{j=1}^{d} n_j \, \partial_{x_j}(\rho u)_i(\tilde{\mathbf{x}}) && \text{second order} \\ &- \|\mathbf{d}\|^2 \sum_{i=1}^{d} n_i \sum_{j=1}^{d} \sum_{k=1}^{d} \frac{1}{2!} \, n_j n_k \, \partial^2_{x_j x_k}(\rho u)_i(\tilde{\mathbf{x}}) && \text{third order} \\ &- \|\mathbf{d}\|^3 \sum_{i=1}^{d} n_i \sum_{j=1}^{d} \sum_{k=1}^{d} \sum_{\ell=1}^{d} \frac{1}{3!} \, n_j n_k n_\ell \, \partial^3_{x_j x_k x_\ell}(\rho u)_i(\tilde{\mathbf{x}}) && \text{fourth order} \\ &\dots , \end{aligned} \tag{29}$$

and (27) by

$$W_{\text{SBM}} = (\rho\mathbf{u})(\tilde{\mathbf{x}})\cdot\mathbf{n} - (\rho\mathbf{u})(\tilde{\mathbf{x}}+\mathbf{d})\cdot\mathbf{n}. \tag{30}$$

As discussed before a fully consistent definition of the flux is obtained by consistently correcting the value of the total enthalpy as in (19), by replacing w with w_{SBM} or with W_{SBM}/ρ depending on the case.

4.3. Other existing approaches

The corrections proposed in the previous paragraph will be compared to the approach proposed by Krivodonova and Berger in [43], referred to as *algorithm I* in the cited reference. The aforementioned approach, along with two more *algorithms*, was introduced by the Krivodonova and Berger to provide improved solutions for two-dimensional slip-wall boundary conditions. Even though, their corrections are limited to two-dimensional domains and slip-wall boundary conditions, we recall for completeness the one that we used herein to make comparisons. More details can also be found in [43].

We start by defining in each quadrature point a special state of primitive variables $\mathbf{U}^b$ and a corresponding numerical flux:

$$\mathbf{U}^b = \begin{pmatrix} \rho^b \\ \mathbf{u}^b \\ p^b \end{pmatrix} = \begin{pmatrix} \rho \\ u_t\,\mathbf{t} \\ p \end{pmatrix}, \qquad \mathbf{F}^{bc}_{\tilde{\mathbf{n}}}(\mathbf{U}^b) = \begin{pmatrix} \rho^b\,(\mathbf{u}^b\cdot\tilde{\mathbf{n}}) \\ \rho^b\,(\mathbf{u}^b\cdot\tilde{\mathbf{n}})\,\mathbf{u}^b + p\,\tilde{\mathbf{n}} \\ \rho^b\,(\mathbf{u}^b\cdot\tilde{\mathbf{n}})\,H^b \end{pmatrix}. \tag{31}$$

Note that [43] contains a typo in the flux expression which does not include the pressure term. Even though the modification introduced in (31) already allows a fair improvement of the discretization error and convergence rate, we will see that this shows some limitations when increasing the accuracy already beyond third order [18].

Remark 2 (Shock limiting). *For simulations with shocks, when the a posteriori limiter marks a cell on the wall boundary as troubled, the boundary conditions must be applied differently since the high order modes are discarded and the solution is updated with a second order finite volume scheme. In this case, we adopt the flux modification* (31)*.*

5. Numerical results

In this Section, we test the new modified boundary treatments with several academic test-cases proving that the new method is able to provide high-order convergence for both far-field and wall boundary conditions on 2D and 3D unstructured meshes. We also show the numerical results obtained on a problem that involves shocks, correctly captured in the framework of ADER-DG methods thanks to our *a posteriori* subcell FV limiting technique. The results are provided with convergence analysis performed with classical and modified boundary conditions, and, when possible, with curvilinear meshes.

5.1. 2D tests with smooth solutions

We start our suite of benchmarks with 2-dimensional tests involving smooth solution profiles; this easily allows to asses the claimed properties of the proposed SBM formulation.

5.1.1. Manufactured solution on 2D curved domains: far-field BC

In order to assess the capability of our new flux correction, we start from a manufactured solution by considering the two-dimensional inhomogeneous Euler equations:

$$\mathbf{U}_t + \nabla \cdot \mathbf{F}(\mathbf{U}) = \mathbf{S}, \qquad \text{with} \qquad \mathbf{S} = \begin{pmatrix} 0.4\,\cos(x+y) \\ 0.6\,\cos(x+y) \\ 0.6\,\cos(x+y) \\ 1.8\,\cos(x+y) \end{pmatrix}. \tag{32}$$

This system has the following exact steady state solution, as given in [51],

$$\rho = 1 + 0.2\,\sin(x+y), \quad u = 1, \quad v = 1, \quad p = 1 + 0.2\,\sin(x+y), \tag{33}$$

which is imposed on the real curved domain as far-field boundary conditions. A very coarse mesh was generated and then refined by splitting. The four nested grids described in Table 1 have been used to perform grid-convergence analysis.

The boundary where the far-field condition is applied will be referred to as Γ_D. We tested the new SBM flux correction on a complicated geometry, taken from [18], that can be described with the following equation written in polar coordinates:

$$\Gamma_D : \begin{pmatrix} x \\ y \end{pmatrix} = r(\alpha,\theta)\begin{pmatrix} \cos\theta \\ \sin\theta \end{pmatrix}, \quad \text{where} \quad r(\alpha,\theta) = r_0\left(1 + \frac{1}{10}\sin(\alpha\theta)\right), \quad r_0, \alpha \in \mathbb{R}, \tag{34}$$

where $r_0 = 1$ and $\alpha = 3$. We refer to Figure 3 for a visual representation.

Since the standard far-field boundary condition is enforced onto a curved boundary, discretized with a polygonal mesh, we expect to have second order of accuracy at best no matter what the degree of the polynomial is and this is well-observed in the top part of Table 2. This problem can be cured with the, however expensive, use of iso-parametric elements and curved meshes. For the sake of completeness we provide throughout this paper also some results on curved meshes, see for example the central part of Table 2, but we underline that our technology for curved meshes

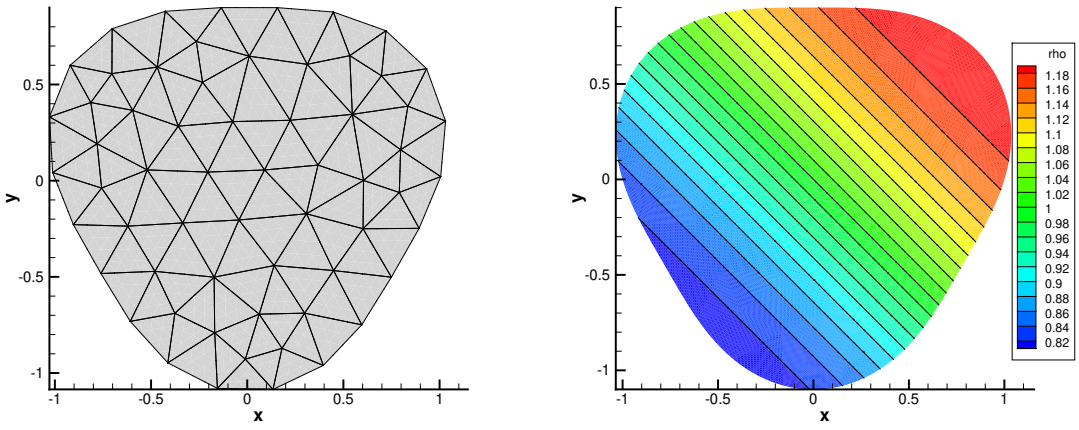

Figure 3: Test case setup for the 2D manufactured solution test case presented in Section 5.1.1. We plot the coarsest employed mesh on the left and the initial density profile on the right.

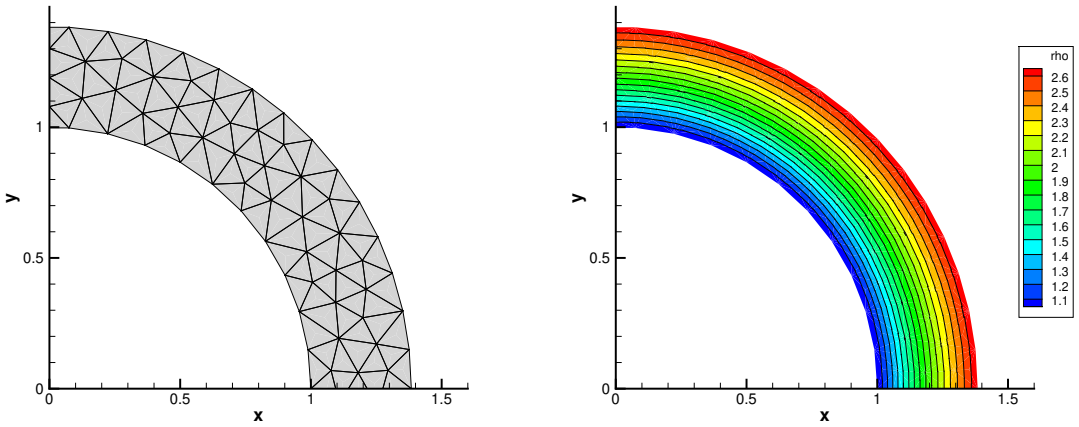

Figure 4: Test case setup for the supersonic vortex bounded by two circular walls presented in Section 5.1.2. We plot the coarsest employed mesh on the left and the initial density profile on the right.

allows to obtain third order accurate results with DG-$\mathbb{P}2/\mathbb{Q}2$ and slightly better results when using DG-$\mathbb{P}3/\mathbb{Q}3$, but without achieving the expected fourth order (however the improvement of curved meshes techniques is not the scope of this work).

Finally, the best results, in terms of error magnitude, convergence rates and reduced computational complexity, are obtained with the shifted boundary correction, as one can see by comparing the previous results with those reported in bottom part of Table 2. Convergence plots[1] until order four, for the conserved variable ρ, are presented in Figure 9a. Although the paper is oriented towards polynomials of degree four, for this test case, we also presented the results obtained using polynomials of degree five to show that, the accuracy of the correction theoretically depends *only* on the order of the polynomial itself. With the SBM correction, all convergence trends are correctly recovered until order five.

5.1.2. Supersonic vortex bounded by two circular walls: slip wall BC

In order to test the new flux corrections for wall boundary conditions, we now consider an isentropic supersonic flow between two concentric circular arcs of radii $r_i = 1$ and $r_o = 1.384$. The exact density in terms of radius r is given by

$$\rho = \rho_i \left(1 + \frac{\gamma + 1}{2} M_i^2 \left(1 - \left(\frac{r_i}{r}\right)^2\right)\right)^{\frac{1}{\gamma - 1}}. \tag{35}$$

The velocity and pressure are given by

$$\|\mathbf{u}\| = \frac{c_i M_i}{r}, \quad p = \frac{\rho^\gamma}{\gamma}, \tag{36}$$

where c_i is the speed of sound on the inner circle. The Mach number on the inner circle M_i is set to 2.25 and the density ρ_i to one. The fluid's velocity vector components in (x, y) can be computed as follows:

$$\begin{pmatrix} u \\ v \end{pmatrix} = \|\mathbf{u}\| \begin{pmatrix} y/r \\ -x/r \end{pmatrix}, \tag{37}$$

where $r = \sqrt{x^2 + y^2}$.

A set of refined meshes is obtained by means of conformal refinement of an initial triangulation shown in Figure 4; the mesh characteristics are given in Table 3. For this test case, we first performed the convergence test by enforcing

[1] For all convergence plots, we draw the dashed lines close to each result ($\mathbb{P}1$, $\mathbb{P}2$, $\mathbb{P}3$) to represent the optimal rate (2, 3, 4) for comparisons.

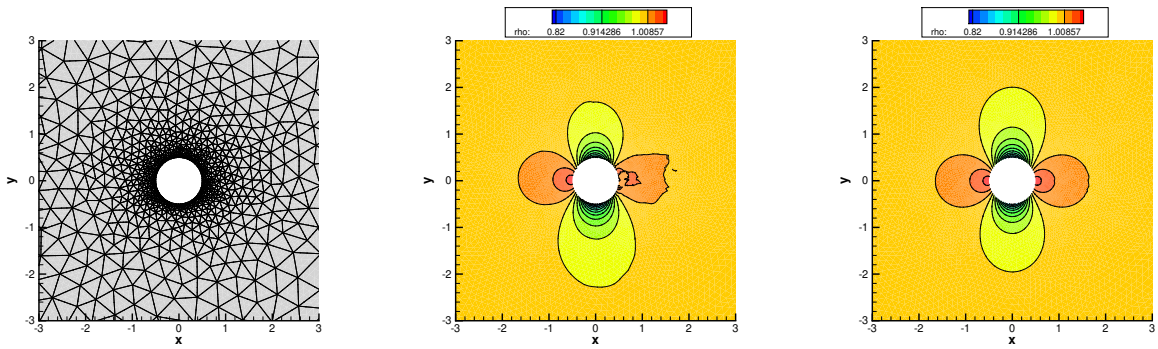

Figure 5: Test case setup for the subsonic flow over a circular cylinder presented in Section 5.1.3. We plot the mesh on the left, the density profile computed with DG-$\mathbb{P}3$ in the middle, and the density profile computed with DG-$\mathbb{P}3$/SBM-$\mathbb{P}3$ on the right.

the standard weak wall boundary condition (given by Equations (17) and (18)) on the polygonal boundary. Table 4 points out the grid-convergence analysis showing that the method is not even able to converge with a full second order rate. It can also be noticed that, for each mesh, the higher is the degree of the polynomial, the larger the error is. This is due to the fact that the scheme is trying to better approximate a solution that is indeed wrong because the boundary, which should be curved, is approximated by a polygon (see Figure 2).

The same test, with the same boundary conditions, has also been run with high order curvilinear meshes showing that when increasing the order of the polynomial used to approximate the boundary we are able to recover the formal order of accuracy of the method, as visible on Table 4. Note that this result is only possible when using iso-parametric elements, so the degree of the polynomial $\mathbb{Q}$ that approximates the geometry and the mesh has to increase with the polynomial $\mathbb{P}$ of the scheme (e.g. DG-$\mathbb{P}1/\mathbb{Q}1$, DG-$\mathbb{P}2/\mathbb{Q}2$, and DG-$\mathbb{P}3/\mathbb{Q}3$). Convergence plots obtained with curvilinear element are shown in Figure 11a for the density variable ρ.

Finally, the results obtained using the SBM corrections on straight sided meshes are reported in Table 6 and shown in Figure 11. The top part of the Table shows the results obtained by using the truncated Taylor series development for the velocity; instead, the bottom part concerns the simplified polynomials correction (30) based on the momentum variables which does not require complex derivative evaluations. We observe the expected rates and low error levels in both cases, with a slight improvement with the simplified approach which may be related to the fact that we are extrapolating the whole ρu_n term, rather than only u_n, as done for the classical SBM formulation (with ρ taken from the quadrature point).

For the sake of completeness, we present in Table 5 and Figure 11b the results obtained with the correction (31). It should be noticed that even for this simple case, considering quadratic geometries, we have an order-of-accuracy degradation for finer meshes when using polynomials of degree higher than two ($\mathbb{P}3$).

5.1.3. Subsonic flow over a circular cylinder: slip wall BC

This test case has the same goal of that presented in [67]: the validation of the new boundary treatment. The free-stream Mach number used in this simulation is 0.3. The comparison was carried by running the most accurate scheme used in this work, DG-$\mathbb{P}3$, with and without the SBM correction to assess the influence of the present approach on this benchmark. We performed the computations with an unstructured Delaunay mesh made by 1,096 nodes and 2,087 triangles. To impose consistent far-field conditions, we have a setup with an outer boundary 20 radiuses away from the cylinder. In order to test the new boundary conditions we studied the symmetry of iso-contours for both density, in Figure 5, and Mach number, in Figure 6. For both variables, a clear improvement of the solution is pointed out by the resuls performed with the SBM correction. Note that, when slip-wall conditions without corrections are considered, the flow is characterized by separation behind the body (see Figure 6a). Instead, a much better prediction of the field is given by the results obtained with the polynomial correction. Finally, in Figure 7, we plot the spurious entropy production generated by the two boundary conditions, indicating a remarkable result also in this case.

Table 1: Characteristics of the employed meshes for the test case of Section 5.1.1, the 2D manufactured solution.

Grid level	Nodes	Triangles	h
0	61	98	1.5450E-1
1	219	392	7.7252E-2
2	829	1,568	3.8626E-2
3	3,225	6,272	1.9313E-2

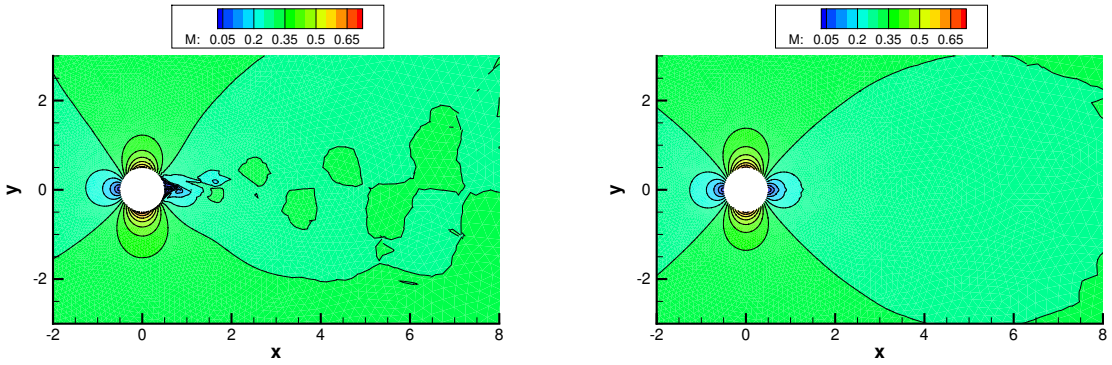

Figure 6: Test case setup for the subsonic flow over a circular cylinder presented in Section 5.1.3. We plot the Mach number profile computed with DG-$\mathbb{P}3$ on the left, and the Mach number profile computed with DG-$\mathbb{P}3$/SBM-$\mathbb{P}3$ on the right.

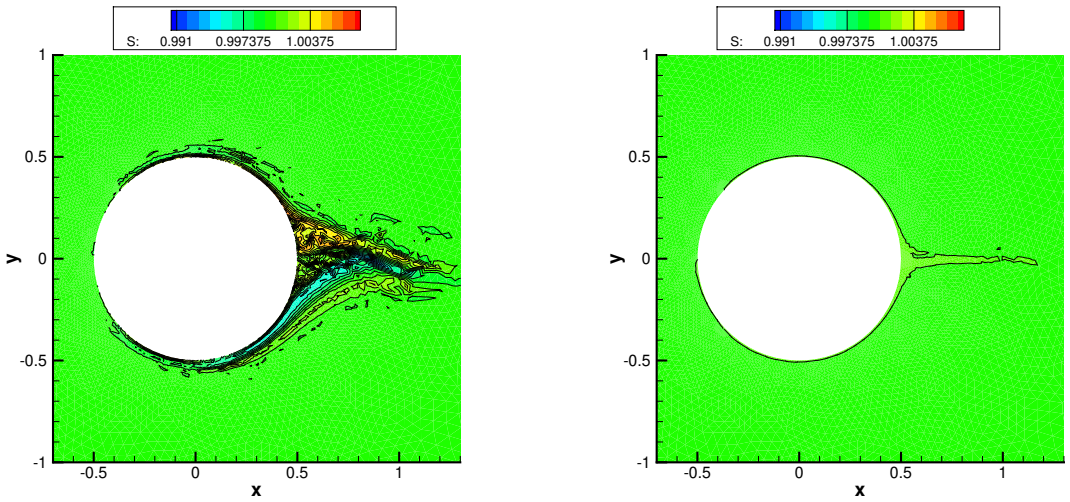

Figure 7: Test case setup for the subsonic flow over a circular cylinder presented in Section 5.1.3. We plot the entropy levels computed with DG-$\mathbb{P}3$ on the left, and the entropy levels computed with DG-$\mathbb{P}3$/SBM-$\mathbb{P}3$ on the right.

Table 2: Convergence analysis for the test case of Section 5.1.1, the 2D manufactured solution. We provide the results obtained without the SBM correction on linear meshes (top part), with curved mesh (central part), and with SBM correction on linear meshes (bottom part). One can notice that the SBM correction allows to retrieve the expected high order convergence rate when working with methods of order greater than 2 on linear meshes.

Convergence analysis *without SBM* correction on *linear* meshes

	ρ		ρu		ρv		ρE	
Grid level	L_2	$\tilde{n}$	L_2	$\tilde{n}$	L_2	$\tilde{n}$	L_2	$\tilde{n}$
				DG-$\mathbb{P}1$				
0	1.7293E-3	–	2.3514E-3	–	2.2344E-3	–	6.6466E-3	–
1	4.4790E-4	1.95	6.0925E-4	1.95	5.7869E-4	1.95	1.7138E-3	1.96
2	1.1276E-4	1.99	1.5358E-4	1.99	1.4579E-4	1.99	4.3195E-4	1.99
3	2.8241E-5	2.00	3.8473E-5	2.00	3.6512E-5	2.00	1.0820E-4	2.00
				DG-$\mathbb{P}2$				
0	1.6583E-3	–	2.3344E-3	–	2.2040E-3	–	6.4258E-3	–
1	4.2195E-4	1.97	5.9156E-4	1.98	5.5908E-4	1.98	1.6308E-3	1.98
2	1.0522E-4	2.00	1.4777E-4	2.00	1.3975E-4	2.00	4.0791E-4	2.00
3	2.6187E-5	2.01	3.6855E-5	2.00	3.4867E-5	2.00	1.0170E-4	2.00
				DG-$\mathbb{P}3$				
0	1.6817E-3	–	2.3809E-3	–	2.2562E-3	–	6.5431E-3	–
1	4.3095E-4	1.96	6.0642E-4	1.97	5.7430E-4	1.97	1.6640E-3	1.98
2	1.0768E-4	2.00	1.5092E-4	2.01	1.4280E-4	2.01	4.1580E-4	2.00
3	2.6792E-5	2.01	3.7467E-5	2.01	3.5428E-5	2.01	1.0345E-4	2.01
				DG-$\mathbb{P}4$				
0	1.6950E-3	–	2.4059E-3	–	2.2813E-3	–	6.5915E-3	–
1	4.3318E-4	1.96	6.1215E-4	1.97	5.8031E-4	1.98	1.6714E-3	1.98
2	1.0849E-4	2.00	1.5293E-4	2.00	1.4497E-4	2.00	4.1861E-4	2.00
3	2.6976E-5	2.00	3.7944E-5	2.01	3.5943E-5	2.01	1.0416E-4	2.00

Convergence analysis on *curved* meshes

	ρ		ρu		ρv		ρE	
Grid level	L_2	$\tilde{n}$	L_2	$\tilde{n}$	L_2	$\tilde{n}$	L_2	$\tilde{n}$
				DG-$\mathbb{P}1/\mathbb{Q}1$				
0	1.7293E-3	–	2.3514E-3	–	2.2344E-3	–	6.6466E-3	–
1	4.4790E-4	1.95	6.0925E-4	1.95	5.7869E-4	1.95	1.7138E-3	1.96
2	1.1276E-4	1.99	1.5358E-4	1.99	1.4579E-4	1.99	4.3195E-4	1.99
3	2.8241E-5	2.00	3.8473E-5	2.00	3.6512E-5	2.00	1.0820E-4	2.00
				DG-$\mathbb{P}2/\mathbb{Q}2$				
0	7.8113E-5	–	4.9287E-5	–	6.0091E-5	–	2.3914E-4	–
1	1.1494E-5	2.76	6.1144E-6	3.01	7.9719E-6	2.91	3.4731E-5	2.78
2	1.5902E-6	2.85	7.8242E-7	2.97	1.0271E-6	2.96	4.7828E-6	2.86
3	2.1096E-7	2.91	1.0184E-7	2.94	1.3078E-7	2.97	6.3447E-7	2.91
				DG-$\mathbb{P}3/\mathbb{Q}3$				
0	5.2248E-6	–	4.7012E-6	–	4.6229E-6	–	1.5742E-5	–
1	5.6390E-7	3.21	4.7322E-7	3.31	4.7014E-7	3.29	1.6226E-6	3.28
2	6.1309E-8	3.20	4.7773E-8	3.31	4.8063E-8	3.29	1.7095E-7	3.25
3	1.0299E-8	2.57	9.2506E-9	2.36	1.0123E-8	2.25	3.6478E-8	2.23

Convergence analysis *with SBM* correction on *linear* meshes

	ρ		ρu		ρv		ρE	
Grid level	L_2	$\tilde{n}$	L_2	$\tilde{n}$	L_2	$\tilde{n}$	L_2	$\tilde{n}$
				DG-$\mathbb{P}1$/SBM-$\mathbb{P}1$				
0	1.0784E-3	–	1.2139E-3	–	1.2479E-3	–	3.3758E-3	–
1	2.3747E-4	2.18	2.4029E-4	2.34	2.4644E-4	2.34	7.2503E-4	2.22
2	5.5268E-5	2.10	5.3230E-5	2.17	5.4522E-5	2.18	1.6929E-4	2.10
3	1.3351E-5	2.05	1.2599E-5	2.08	1.2898E-5	2.08	4.1189E-5	2.04
				DG-$\mathbb{P}2$/SBM-$\mathbb{P}2$				
0	7.5258E-5	–	5.0257E-5	–	5.8531E-5	–	2.2711E-4	–
1	1.1105E-5	2.76	5.6058E-6	3.16	7.1750E-6	3.03	3.2987E-5	2.78
2	1.5701E-6	2.82	7.2761E-7	2.95	9.2582E-7	2.95	4.6465E-6	2.83
3	2.1377E-7	2.88	1.0003E-7	2.86	1.1793E-7	2.97	6.3270E-7	2.88
				DG-$\mathbb{P}3$/SBM-$\mathbb{P}3$				
0	1.7331E-6	–	2.8523E-6	–	2.9879E-6	–	6.3787E-6	–
1	7.0445E-8	4.62	9.8935E-8	4.85	1.0298E-7	4.86	2.3519E-7	4.76
2	3.2654E-9	4.43	3.9178E-9	4.66	4.0466E-9	4.67	1.0200E-8	4.53
3	1.7487E-10	4.22	1.8709E-10	4.39	1.9248E-10	4.39	5.3564E-10	4.25
				DG-$\mathbb{P}4$/SBM-$\mathbb{P}4$				
0	4.4808E-8	–	4.9888E-8	–	5.3190E-8	–	1.4804E-7	–
1	1.2360E-9	5.18	9.2420E-10	5.75	1.0080E-9	5.72	3.8553E-9	5.26
2	4.0526E-11	4.93	2.5906E-11	5.16	2.7614E-11	5.19	1.2496E-10	4.95
3	–	–	–	–	–	--	–	–

Table 3: Characteristics of the employed meshes for the test case of Section 5.1.2.

Grid level	Nodes	Triangles	h
0	238	376	1.024E-01
1	852	1,504	5.121E-02
2	3,208	6,016	2.560E-02
3	12,432	24,064	1.280E-02

Table 4: Convergence analysis for the test case of Section 5.1.2, the supersonic vortex bounded by two circular walls in 2D, performed *with* linear and curved elements without the SBM correction.

Convergence analysis *without SBM* correction on *linear* meshes.

	ρ		ρu		ρv		ρE	
Grid level	L_2	$\tilde{n}$	L_2	$\tilde{n}$	L_2	$\tilde{n}$	L_2	$\tilde{n}$
				DG-$\mathbb{P}1$				
0	4.0507E-2	–	5.9773E-2	–	6.0006E-2	–	1.7033E-1	–
1	1.3141E-2	1.62	1.9227E-2	1.64	1.9330E-2	1.63	5.6565E-2	1.59
2	4.4645E-3	1.56	6.5585E-3	1.55	6.5822E-3	1.55	1.9499E-2	1.54
3	1.5786E-3	1.50	2.3646E-3	1.47	2.3684E-3	1.47	6.9664E-3	1.48
				DG-$\mathbb{P}2$				
0	7.5758E-2	–	1.3956E-1	–	1.4152E-1	–	3.3516E-1	–
1	2.7584E-2	1.46	5.1868E-2	1.43	5.1990E-2	1.44	1.2308E-1	1.45
2	9.6935E-3	1.51	1.8547E-2	1.48	1.8548E-2	1.49	4.3649E-2	1.50
3	3.4687E-3	1.48	6.5731E-3	1.50	6.5656E-3	1.50	1.5548E-2	1.49
				DG-$\mathbb{P}3$				
0	1.9104E-1	–	2.2847E-1	–	2.2992E-1	–	7.2469E-1	–
1	8.3972E-2	1.19	9.9892E-2	1.19	1.0244E-1	1.17	3.2130E-1	1.17
2	3.5508E-2	1.24	4.0370E-2	1.31	4.1040E-2	1.32	1.3453E-1	1.26
3	1.5314E-2	1.21	1.6278E-2	1.31	1.6507E-2	1.31	5.7225E-2	1.23

Convergence analysis on *curved* meshes

	ρ		ρu		ρv		ρE	
Grid level	L_2	$\tilde{n}$	L_2	$\tilde{n}$	L_2	$\tilde{n}$	L_2	$\tilde{n}$
				DG-$\mathbb{P}1/\mathbb{Q}1$				
0	4.0507E-2	–	5.9773E-2	–	6.0006E-2	–	1.7033E-1	–
1	1.3141E-2	1.62	1.9227E-2	1.64	1.9330E-2	1.63	5.6565E-2	1.59
2	4.4645E-3	1.56	6.5585E-3	1.55	6.5822E-3	1.55	1.9499E-2	1.54
3	1.5786E-3	1.50	2.3646E-3	1.47	2.3684E-3	1.47	6.9664E-3	1.48
				DG-$\mathbb{P}2/\mathbb{Q}2$				
0	1.2075E-3	–	1.7408E-3	–	1.7527E-3	–	4.8709E-3	–
1	1.9156E-4	2.66	2.6389E-4	2.72	2.6721E-4	2.71	7.7666E-4	2.65
2	2.5831E-5	2.89	3.3546E-5	2.98	3.3662E-5	2.99	1.0323E-4	2.91
3	3.0727E-6	3.07	4.1031E-6	3.03	4.0812E-6	3.04	1.2467E-5	3.05
				DG-$\mathbb{P}3/\mathbb{Q}3$				
0	7.0183E-5	–	8.8438E-5	–	8.9166E-5	–	2.7348E-4	–
1	4.8983E-6	3.84	6.7326E-6	3.72	6.7616E-6	3.72	1.9264E-5	3.83
2	4.0876E-7	3.58	5.9445E-7	3.50	5.9936E-7	3.50	1.6698E-6	3.50
3	3.2822E-8	3.64	5.1193E-8	3.54	5.1593E-8	3.54	1.3795E-7	3.60

Table 5: Convergence analysis for the test case of Section 5.1.2, the supersonic vortex bounded by two circular walls in 2D, with the modified flux introduced in (31).

	ρ		ρu		ρv		ρE	
Grid level	L_2	$\tilde{n}$	L_2	$\tilde{n}$	L_2	$\tilde{n}$	L_2	$\tilde{n}$
				DG-$\mathbb{P}1$ with correction (31)				
0	1.9580E-2	–	4.1681E-2	–	4.1868E-2	–	8.9637E-2	–
1	5.3355E-3	1.88	1.1620E-2	1.84	1.1676E-2	1.84	2.4676E-2	1.86
2	1.1690E-3	2.19	2.5781E-3	2.17	2.5983E-3	2.17	5.3291E-3	2.21
3	2.4711E-4	2.24	5.5186E-4	2.22	5.5738E-4	2.22	1.0988E-3	2.28
				DG-$\mathbb{P}2$ with correction (31)				
0	1.2764E-3	–	1.8543E-3	–	1.8656E-3	–	5.2077E-3	–
1	1.9749E-4	2.69	2.6604E-4	2.80	2.6928E-4	2.79	7.9744E-4	2.71
2	2.5994E-5	2.92	3.3359E-5	2.99	3.3458E-5	3.00	1.0360E-4	2.94
3	3.0959E-6	3.06	4.1008E-6	3.02	4.0776E-6	3.03	1.2531E-5	3.04
				DG-$\mathbb{P}3$ with correction (31)				
0	8.3269E-5	–	1.0748E-4	–	1.0489E-4	–	3.2138E-4	–
1	5.3483E-6	3.96	6.6779E-6	4.00	6.5981E-6	3.99	2.0358E-5	3.98
2	4.6348E-7	3.52	5.0053E-7	3.73	5.0276E-7	3.71	1.7297E-6	3.55
3	4.5383E-8	3.35	4.3567E-8	3.52	4.3975E-8	3.51	1.6679E-7	3.37

Table 6: Convergence analysis for the test case of Section 5.1.2, the supersonic vortex bounded by two circular walls in 2D, performed *with* the use of SBM corrections on linear meshes. We provide the results obtained with the entire Taylor series evaluation of Eq. (26) (top part of the Table) and those obtained with the simplified formula of Eq. (30) (bottom part of the Table).

Convergence analysis *with SBM* correction, as given in Eq. (26)

	ρ		ρu		ρv		ρE	
Grid level	L_2	$\tilde{n}$	L_2	$\tilde{n}$	L_2	$\tilde{n}$	L_2	$\tilde{n}$
				DG-$\mathbb{P}1$/SBM-$\mathbb{P}1$				
0	1.6446E-2	–	3.5594E-2	–	3.5415E-2	–	7.7895E-2	–
1	4.5403E-3	1.86	9.9195E-3	1.84	9.9279E-3	1.84	2.1613E-2	1.85
2	9.5300E-4	2.25	2.0713E-3	2.26	2.0770E-3	2.26	4.5047E-3	2.26
3	1.9068E-4	2.32	4.1246E-4	2.33	4.1396E-4	2.33	8.9777E-4	2.33
				DG-$\mathbb{P}2$/SBM-$\mathbb{P}2$				
0	1.2652E-3	–	1.8623E-3	–	1.8779E-3	–	5.2247E-3	–
1	1.9622E-4	2.69	2.6306E-4	2.82	2.6695E-4	2.81	7.9217E-4	2.72
2	2.5770E-5	2.93	3.3068E-5	2.99	3.3222E-5	3.01	1.0284E-4	2.95
3	3.0587E-6	3.08	4.0533E-6	3.03	4.0349E-6	3.04	1.2390E-5	3.05
				DG-$\mathbb{P}3$/SBM-$\mathbb{P}3$				
0	6.2321E-5	–	9.0618E-5	–	8.7148E-5	–	2.4363E-4	–
1	2.9113E-6	4.42	4.9355E-6	4.20	4.7997E-6	4.18	1.1976E-5	4.35
2	1.5293E-7	4.25	2.6814E-7	4.20	2.6463E-7	4.18	6.3695E-7	4.23
3	8.5252E-9	4.17	1.4884E-8	4.17	1.4727E-8	4.17	3.5447E-8	4.17

Convergence analysis *with SBM* correction, as given in Eq. (30)

	ρ		ρu		ρv		ρE	
Grid level	L_2	$\tilde{n}$	L_2	$\tilde{n}$	L_2	$\tilde{n}$	L_2	$\tilde{n}$
				DG-$\mathbb{P}1$/SBM-$\mathbb{P}1$				
0	1.6335E-2	–	3.5355E-2	–	3.5183E-2	–	7.7374E-2	–
1	4.5259E-3	1.85	9.8900E-3	1.84	9.8996E-3	1.84	2.1548E-2	1.84
2	9.5188E-4	2.25	2.0689E-3	2.26	2.0748E-3	2.26	4.4993E-3	2.26
3	1.9058E-4	2.32	4.1225E-4	2.33	4.1376E-4	2.33	8.9728E-4	2.33
				DG-$\mathbb{P}2$/SBM-$\mathbb{P}2$				
0	1.2604E-3	–	1.8419E-3	–	1.8568E-3	–	5.1834E-3	–
1	1.9606E-4	2.69	2.6221E-4	2.82	2.6608E-4	2.81	7.9063E-4	2.72
2	2.5765E-5	2.93	3.3039E-5	2.99	3.3192E-5	3.01	1.0279E-4	2.95
3	3.0584E-6	3.08	4.0524E-6	3.03	4.0340E-6	3.04	1.2388E-5	3.05
				DG-$\mathbb{P}3$/SBM-$\mathbb{P}3$				
0	6.2289E-5	–	9.1157E-5	–	8.7853E-5	–	2.4332E-4	–
1	2.8518E-6	4.45	4.9380E-6	4.20	4.7981E-6	4.19	1.1777E-5	4.37
2	1.4569E-7	4.29	2.6571E-7	4.22	2.6206E-7	4.19	6.1275E-7	4.26
3	7.9556E-9	4.20	1.4647E-8	4.18	1.4496E-8	4.18	3.3523E-8	4.19

Table 7: Characteristics of the employed meshes for the test case of Section 5.2.1, the 3D manufactured solution.

Grid level	Nodes	Tetrahedra	h
0	169	778	2.8274E-01
1	971	5,072	1.4137E-01
2	6,437	35,968	7.0686E-02

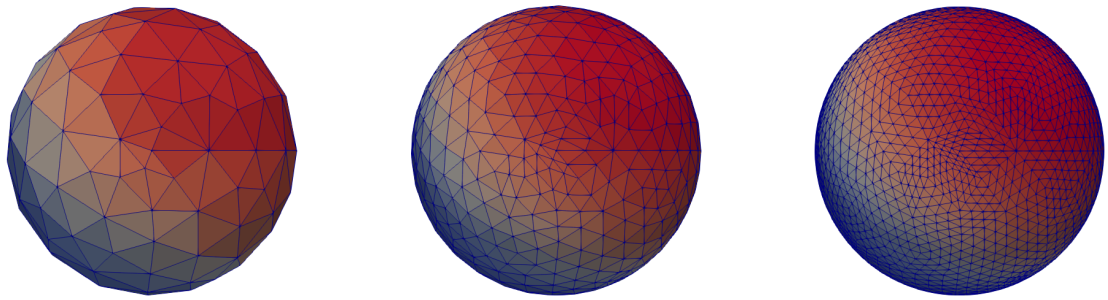

(a) Grid level 0 (b) Grid level 1 (c) Grid level 2

Figure 8: Test case setup for the 3D manufactured solution test case presented in Section 5.2.1.

5.2. 3D tests with smooth solutions

We repeat the same study of the previous Section in the three-dimensional case.

5.2.1. Manufactured solution on 3D curved domains: far-field BC

First, we consider the three-dimensional inhomogeneous Euler equations:

$$\mathbf{U}_t + \nabla \cdot \mathbf{F}(\mathbf{U}) = \mathbf{S}, \qquad \text{with} \qquad \mathbf{S} = \begin{pmatrix} 0.6\,\cos(x+y+z) \\ 0.8\,\cos(x+y+z) \\ 0.8\,\cos(x+y+z) \\ 0.8\,\cos(x+y+z) \\ 3.0\,\cos(x+y+z) \end{pmatrix}. \tag{38}$$

This system has the following exact steady state solution, recovered using the *manufactured solution technique*,

$$\rho = 1 + 0.2\,\sin(x+y+z), \quad u = 1, \quad v = 1, \quad \omega = 1, \quad p = 1 + 0.2\,\sin(x+y+z), \tag{39}$$

which is imposed on the domain boundaries as far-field boundary conditions.

A sphere is now considered as boundary of the domain which introduces an error when using linear meshes due to the curvature. The employed linear meshes are shown in Figure 8. As expected when applying the far-field condition on the real curved boundary, the geometrical error given by the linear mesh overcomes by far that given by the discretization technique with the outcome that no better than second order of accuracy can be achieved (see Table 8). As before better results are obtained when using the SBM correction, indeed high order convergence is well recovered, as shown in Table 8. Again, convergence plots for the conserved variable ρ are presented in Figure 9b.

5.2.2. Supersonic vortex bounded by two cylindrical walls: slip wall BC

We consider a 3D isentropic supersonic flow between two concentric cylindrical surfaces of radii $r_i = 1$ and $r_o = 1.384$. The exact density, velocity and pressure in terms of radius r are given by Eqs. (35) and (36) and the

Table 8: Convergence analysis for the test case of Section 5.2.1, the 3D manufactured solution. We provide the results obtained without the SBM correction on linear meshes (top part) and with SBM correction on linear meshes (bottom part).

Convergence analysis *without SBM* correction on *linear* meshes

	ρ		ρu		ρv		$\rho\omega$		ρE	
Grid level	L_2	$\tilde{n}$	L_2	$\tilde{n}$	L_2	$\tilde{n}$	L_2	$\tilde{n}$		
					DG-$\mathbb{P}1$					
0	8.7027E-3	–	8.8173E-3	–	8.8456E-3	–	8.7977E-3	–	3.3551E-2	–
1	2.4345E-3	1.84	2.4372E-3	1.86	2.4416E-3	1.86	2.4330E-3	1.85	9.3166E-3	1.85
2	6.7942E-4	1.84	6.7824E-4	1.85	6.8014E-4	1.84	6.7829E-4	1.84	2.6093E-3	1.84
					DG-$\mathbb{P}2$					
0	7.6027E-4	–	9.1039E-4	–	8.9306E-4	–	8.4296E-4	–	3.2308E-3	–
1	1.7566E-4	2.11	2.1977E-4	2.05	2.1528E-4	2.05	1.9975E-4	2.08	7.8918E-4	2.03
2	4.2006E-5	2.06	5.4457E-5	2.01	5.3289E-5	2.01	4.8978E-5	2.03	1.9422E-4	2.02
					DG-$\mathbb{P}3$					
0	6.9598E-4	–	8.7766E-4	–	8.5810E-4	–	7.9330E-4	–	3.1103E-3	–
1	1.6687E-4	2.06	2.1777E-4	2.01	2.1300E-4	2.01	1.9540E-4	2.02	7.7173E-4	2.01
2	4.1490E-5	2.01	5.4856E-5	1.99	5.3567E-5	1.99	4.9074E-5	1.99	1.9345E-4	2.00

Convergence analysis *with SBM* correction on *linear* meshes

	ρ		ρu		ρv		$\rho\omega$		ρE	
Grid level	L_2	$\tilde{n}$	L_2	$\tilde{n}$	L_2	$\tilde{n}$	L_2	$\tilde{n}$		
					DG-$\mathbb{P}1$/SBM-$\mathbb{P}1$					
0	9.0767E-3	–	9.1066E-3	–	9.1410E-3	–	9.1148E-3	–	3.5055E-2	–
1	2.4981E-3	1.86	2.4841E-3	1.87	2.4895E-3	1.88	2.4859E-3	1.87	9.5724E-3	1.87
2	6.9067E-4	1.85	6.8601E-4	1.86	6.8798E-4	1.86	6.8738E-4	1.85	2.6541E-3	1.85
					DG-$\mathbb{P}2$/SBM-$\mathbb{P}2$					
0	3.2537E-4	–	3.3772E-4	–	3.4049E-4	–	3.3983E-4	–	1.2000E-3	–
1	4.5765E-5	2.83	4.5417E-5	2.89	4.5165E-5	2.91	4.5562E-5	2.90	1.8400E-4	2.71
2	7.8831E-6	2.54	7.4985E-6	2.60	7.4576E-6	2.60	7.5288E-6	2.60	2.9674E-5	2.63
					DG-$\mathbb{P}3$/SBM-$\mathbb{P}3$					
0	2.0810E-5	–	2.3072E-5	–	2.3226E-5	–	2.2280E-5	–	8.4229E-5	–
1	1.3956E-6	3.90	1.4671E-6	3.98	1.4566E-6	4.00	1.4633E-6	3.93	5.5552E-6	3.92
2	1.3372E-7	3.38	1.3562E-7	3.44	1.3579E-7	3.42	1.3562E-7	3.43	5.1363E-7	3.44

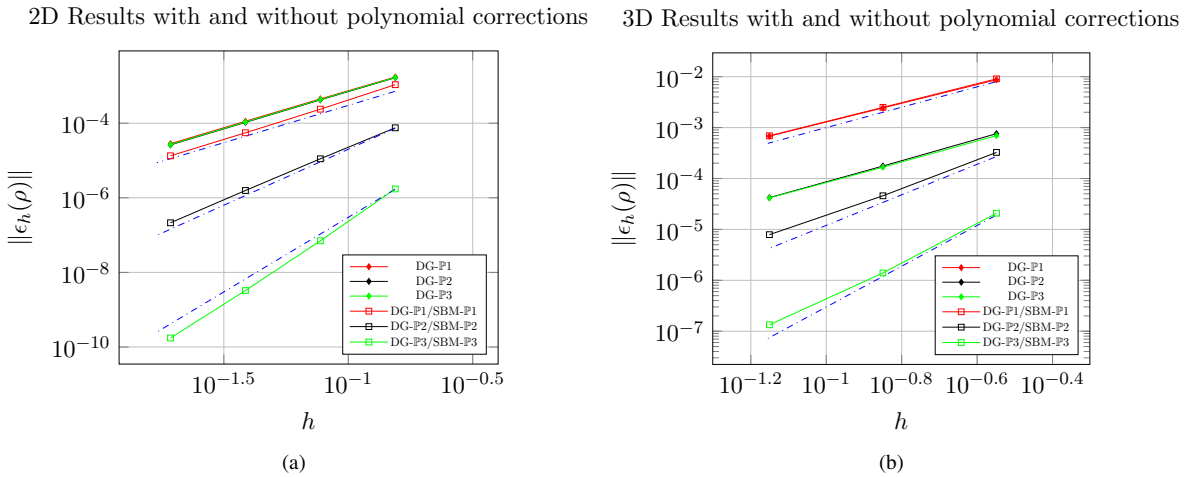

Figure 9: Manufactured solution (2D/3D): results obtained with and without the SBM correction.

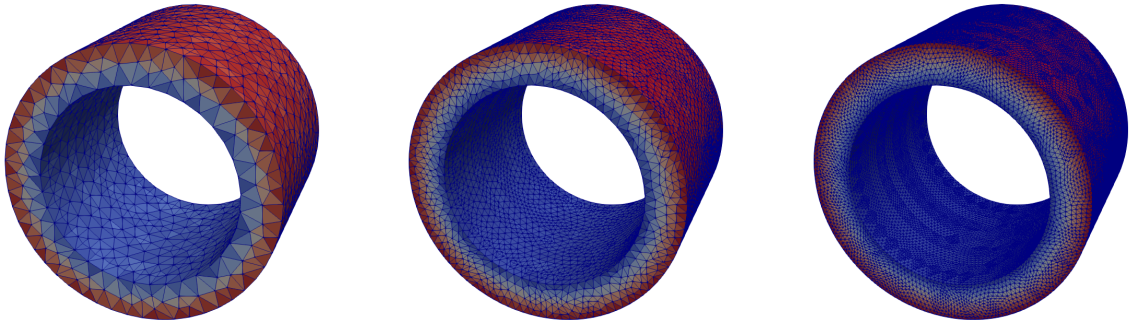

(a) Grid level 0 (b) Grid level 1 (c) Grid level 2

Figure 10: Supersonic vortex bounded by two cylindrical walls (3D): density contours.

solution in the inner surface is taken as that in Section 5.1.2. The fluid's velocity vector components in (x, y, z) can be computed as follows:

$$\begin{pmatrix} u \\ v \\ \omega \end{pmatrix} = \|\mathbf{u}\| \begin{pmatrix} y/r \\ -x/r \\ 0 \end{pmatrix}, \tag{40}$$

where $r = \sqrt{x^2 + y^2}$ because the cylindrical surfaces are developed along the z–axis.

Simulations are first run with classical reflecting wall boundary conditions applied on the approximated boundary. The results presented in Table 10 show convergence trends of rates between 1.5 and 1 for all high order polynomials. Finally, Table 10 presents the results obtained using the SBM wall flux correction: already a little improvement is shown for $\mathbb{P}1$ and for higher order all convergence trends are properly recovered (see Figure 11d for the convergences plot for the density variable ρ).

Table 9: Characteristics of the employed meshes for the test case of Section 5.2.2, the supersonic vortex bounded by two cylindrical walls in 3D.

Grid level	Nodes	Tetrahedra	h
0	3,071	13,059	1.0382E-01
1	20,929	104,472	5.2221E-02
2	153,242	835,776	2.6112E-02

5.3. Shock-cylinder interaction

The last test case we want to address here consider the interaction of a shock wave with a two-dimensional cylinder. The computational domain is $[-2, 6]\times[-3, 3]$ discretized with an unstructured triangulation made by 7,761 grid points and 15,198 elements. The employed ADER-DG scheme is supplemented with the *a posteriori* sub-cell finite volume limiter. The cylinder is centered in $(0, 0)$ and has radius 0.5. The initial condition consists in a shock wave traveling at *Mach number* $M_s = 1.3$ and is then given via the Rankine-Hugoniot conditions. The flow upstream the shock is at rest and is characterized by density and pressure, respectively being $\rho = 1.4$ and $p = 1$. The simulation has been run with polynomials $\mathbb{P}1$, $\mathbb{P}2$ and $\mathbb{P}3$ comparing the implemented wall boundary conditions, with and without the SBM flux correction. Figure 12 shows the initial condition for the Mach number distribution. The time evolution is then shown in Figure 13 where again we plot the Mach number distribution computed with the DG-$\mathbb{P}3$ polynomials comparing the results obtained with and without the SBM correction. We already observe a notable improvement in the iso-contours close to the cylinder in Figure 13. Regarding the limiter activations, it should be noticed that no fundamental difference is observed for the classical and new wall boundary conditions. Finally, in Figure 14 we present a summary of the obtained solutions around the body with different methods. We can observe that by increasing the order of the

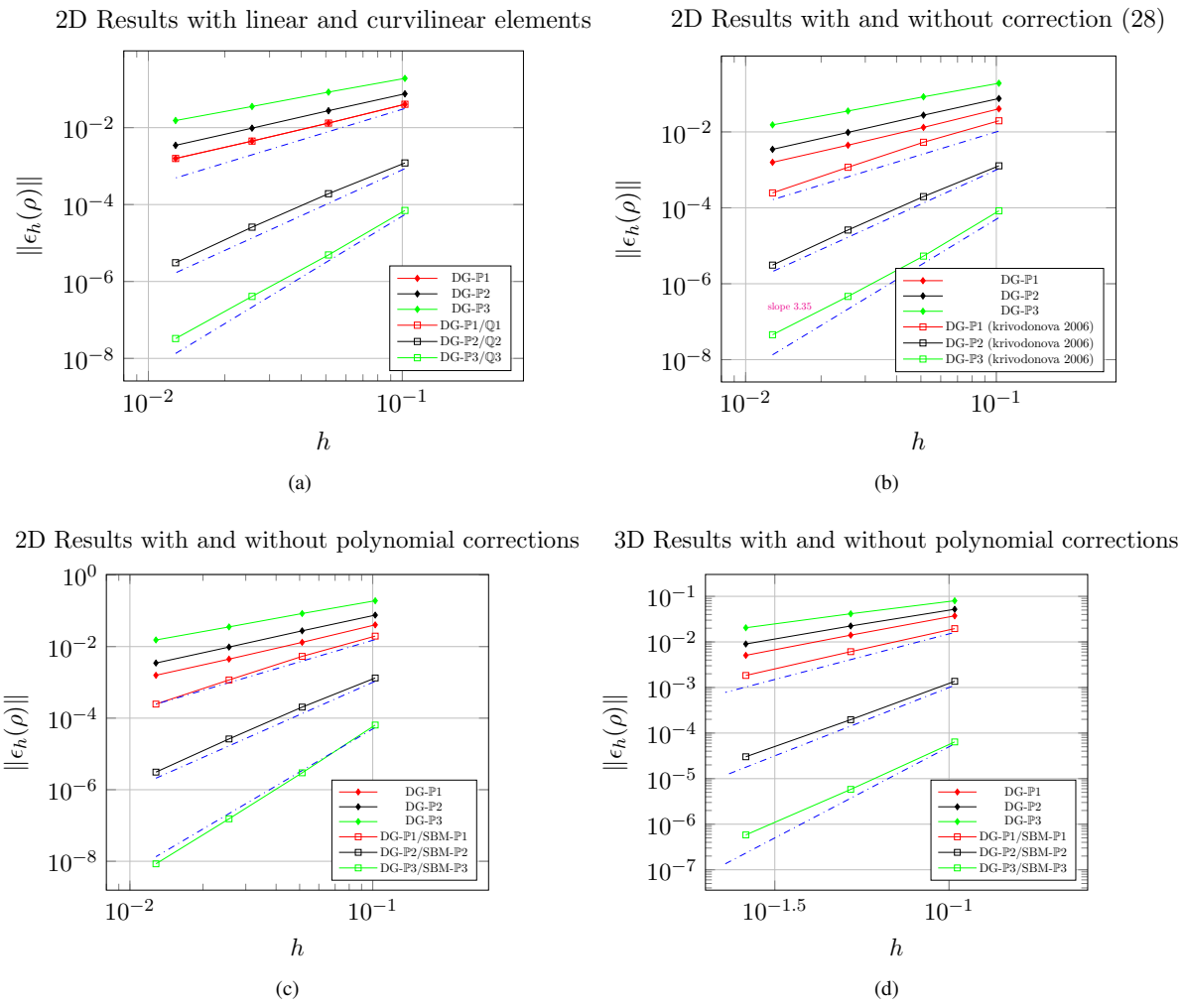

Figure 11: Supersonic vortex bounded by two walls (2D/3D): convergence tests performed with (a) linear and curvilinear 2D grids; (b) wall correction provided in (31); (c) polynomial corrections for 2D grids; (d) polynomial corrections for 3D grids.

Table 10: Convergence analysis for the test case of Section 5.2.2, the supersonic vortex bounded by two cylindrical walls in 3D. We provide the results obtained without the SBM correction on linear meshes (top part) and with SBM correction on linear meshes (bottom part).

Convergence analysis *without SBM* correction on *linear* meshes

	ρ		ρu		ρv		$\rho\omega$		ρE	
Grid level	L_2	$\tilde{n}$	L_2	$\tilde{n}$	L_2	$\tilde{n}$	L_2	$\tilde{n}$		
					DG-$\mathbb{P}1$					
0	3.7322E-2	–	6.4933E-2	–	6.5061E-2	–	1.1475E-2	–	1.6600E-1	–
1	1.4081E-2	1.41	2.0592E-2	1.65	2.0796E-2	1.65	5.0424E-3	1.18	6.0193E-2	1.46
2	5.0733E-3	1.47	6.6189E-3	1.64	6.7225E-3	1.63	1.9803E-3	1.35	2.1242E-2	1.50
					DG-$\mathbb{P}2$					
0	5.2040E-2	–	5.9910E-2	–	6.1607E-2	–	1.6668E-2	–	2.0989E-1	–
1	2.2376E-2	1.22	2.3548E-2	1.35	2.4191E-2	1.35	8.6415E-3	0.95	8.6540E-2	1.28
2	9.0045E-3	1.31	8.8598E-3	1.41	9.1564E-3	1.40	3.8322E-3	1.17	3.4325E-2	1.33
					DG-$\mathbb{P}3$					
0	8.0027E-2	–	8.787E-2	–	8.9290E-2	–	2.5696E-2	–	3.0165E-1	–
1	4.1512E-2	0.94	3.931E-2	1.16	4.0139E-2	1.15	1.5240E-2	0.75	1.5087E-1	1.00
2	2.0451E-2	1.02	1.729E-2	1.18	1.7731E-2	1.18	8.3006E-3	0.87	7.3682E-2	1.03

Convergence analysis *with SBM* correction on *linear* meshes

	ρ		ρu		ρv		$\rho\omega$		ρE	
Grid level	L_2	$\tilde{n}$	L_2	$\tilde{n}$	L_2	$\tilde{n}$	L_2	$\tilde{n}$		
					DG-$\mathbb{P}1$/SBM-$\mathbb{P}1$					
0	1.9580E-2	–	5.4668E-2	–	5.3611E-2	–	5.8383E-3	–	9.1443E-2	–
1	6.1094E-3	1.68	1.5653E-2	1.80	1.5334E-2	1.80	2.0797E-3	1.49	2.7820E-2	1.72
2	1.8376E-3	1.73	4.4901E-3	1.80	4.4063E-3	1.80	7.0284E-4	1.57	8.2183E-3	1.76
					DG-$\mathbb{P}2$/SBM-$\mathbb{P}2$					
0	1.3668E-3	–	2.4856E-3	–	2.4388E-3	–	6.4125E-4	–	6.3670E-3	–
1	1.9656E-4	2.80	3.6385E-4	2.77	3.5349E-4	2.79	9.7458E-5	2.72	9.2034E-4	2.79
2	3.0200E-5	2.70	5.3739E-5	2.76	5.2281E-5	2.75	1.5670E-5	2.64	1.3566E-4	2.76
					DG-$\mathbb{P}3$/SBM-$\mathbb{P}3$					
0	6.3903E-5	–	1.0992E-4	–	1.0858E-4	–	2.7024E-5	–	2.6291E-4	–
1	5.8075E-6	3.46	1.0098E-5	3.44	9.9331E-6	3.45	2.3153E-6	3.54	2.3666E-5	3.47
2	5.8223E-7	3.32	1.0373E-6	3.28	1.0171E-6	3.29	2.3309E-7	3.31	2.3781E-6	3.31

polynomials the results obtained with classical wall boundary conditions get worse and the SBM flux correction really introduces a notable improvement.

6. Conclusions

In this work we have provided a novel effective approach to handle boundary conditions with arbitrary high order of accuracy for curved domain discretized through DG schemes on simple linear meshes. The proposed strategy relies on the shifted boundary method that allows to overcome the second-order geometrical error due to the inconsistent treatment of curved boundaries thanks to a polynomial correction of the boundary condition and the boundary flux, without being obliged to manage curvilinear meshes and the difficulties that go with that (mesh generation process, isoparametric transformation and special quadrature formulas).

In particular, as remarked in section 4.1, the original SBM approximation corresponds to a local change in basis functions at each quadrature point which is expensive when increasing the approximation order, and moreover unnecessary. The approach used here is based on the use of the available polynomial bases, whatever they are, at all quadrature points. The new approach has been tested over a large set of benchmarks in 2D and 3D and with both steady and unsteady flows. The formal order of accuracy provided by the employed DG-$\mathbb{P}N$ schemes has been numerically retrieved in all the performed test cases, and furthermore, the boundary corrections have also been coupled with the *a posteriori* subcell FV limiter, thus allowing the effective simulation of shocks and discontinuities.

Further extensions of the present work will concern first of all its application in the context of moving meshes and moving interfaces [34], and then the additional development necessary for its usage in fully embedded computations [54, 44], which do not require any conformal meshing of internal boundaries. Finally, we also plan to use a similar approach in the context of more complex models as Navier-Stokes equations, for which the extension should be straightforward, the MHD equations [29] where also the magnetic field should be correctly handled, up to the GPR unified model of continuum mechanics [27] for which also the distortion field should be taken into account.

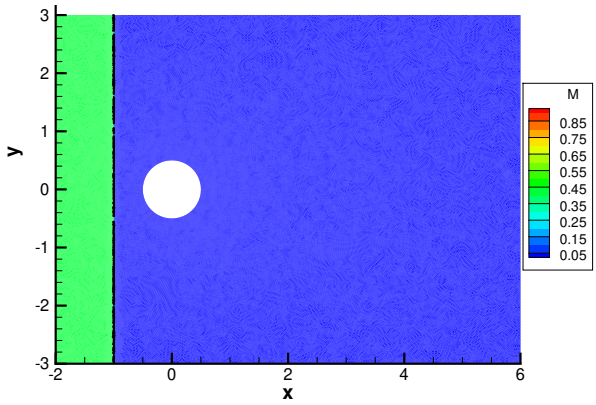

Figure 12: Test case setup for the shock-cylinder interaction of Section 5.3. We show the initial Mach number profile at time $t = 0$.

Acknowledgments

The authors are members of the CARDAMOM team in the Inria center at the University of Bordeaux. E. G. gratefully acknowledges the support received from the European Union's Horizon 2020 Research and Innovation Programme under the Marie Skłodowska-Curie Individual Fellowship *SuPerMan*, grant agreement No. 101025563. The numerical simulations presented in this paper were carried out using the PlaFRIM experimental testbed, supported by Inria, CNRS (LABRI and IMB), Université de Bordeaux, Bordeaux INP and Conseil Régional d'Aquitaine (see https://www.plafrim.fr/).

References

[1] A. Assonitis, M. Ciallella, R. Paciorri, M. Ricchiuto, and A. Bonfiglioli. A new shock-fitting technique for 2-d structured grids. In *AIAA Scitech 2022 Forum*, page 2008, 2022.

[2] N. M. Atallah, C. Canuto, and G. Scovazzi. The high-order shifted boundary method and its analysis. *Computer Methods in Applied Mechanics and Engineering*, 394:114885, 2022.

[3] D. S. Balsara, T. Rumpf, M. Dumbser, and C.-D. Munz. Efficient, high accuracy ader-weno schemes for hydrodynamics and divergence-free magnetohydrodynamics. *Journal of Computational Physics*, 228(7):2480–2516, 2009.

[4] F. Bassi and S. Rebay. Accurate 2d euler computations by means of a high order discontinuous finite element method. In *Fourteenth International Conference on Numerical Methods in Fluid Dynamics*, pages 234–240. Springer, 1995.

[5] F. Bassi and S. Rebay. High-order accurate discontinuous finite element solution of the 2d euler equations. *Journal of computational physics*, 138(2):251–285, 1997.

[6] W. Boscheri, S. Chiocchetti, and I. Peshkov. A cell-centered implicit-explicit lagrangian scheme for a unified model of nonlinear continuum mechanics on unstructured meshes. *Journal of Computational Physics*, 451:110852, 2022.

[7] W. Boscheri, M. Dumbser, R. Loubère, and P.-H. Maire. A second-order cell-centered lagrangian ader-mood finite volume scheme on multidimensional unstructured meshes for hydrodynamics. *Journal of Computational Physics*, 358:103–129, 2018.

[8] W. Boscheri and R. Loubère. High order accurate direct Arbitrary-Lagrangian–Eulerian ADER-MOOD finite volume schemes for non-conservative hyperbolic systems with stiff source terms. *Communications in Computational Physics*, 21(1):271–312, 2017.

[9] W. Boscheri, R. Loubere, and M. Dumbser. Direct Arbitrary-Lagrangian–Eulerian ADER-MOOD finite volume schemes for multidimensional hyperbolic conservation laws. *Journal of Computational Physics*, 292:56–87, 2015.

[10] S. Busto, M. Tavelli, W. Boscheri, and M. Dumbser. Efficient high order accurate staggered semi-implicit discontinuous Galerkin methods for natural convection problems. *Computers & Fluids*, 198:104399, 2020.

[11] J. C. Butcher. Numerical methods for ordinary differential equations in the 20th century. *Journal of Computational and Applied Mathematics*, 125(1-2):1–29, 2000.

[12] N. Chalmers and L. Krivodonova. A robust cfl condition for the discontinuous Galerkin method on triangular meshes. *Journal of Computational Physics*, 403:109095, 2020.

[13] S. Chiocchetti, I. Peshkov, S. Gavrilyuk, and M. Dumbser. High order ADER schemes and GLM curl cleaning for a first order hyperbolic formulation of compressible flow with surface tension. *Journal of Computational Physics*, 426:109898, 2021.

[14] M. Ciallella, M. Ricchiuto, R. Paciorri, and A. Bonfiglioli. Extrapolated discontinuity tracking for complex 2d shock interactions. *Computer Methods in Applied Mechanics and Engineering*, 391:114543, 2022.

[15] S. Clain, S. Diot, and R. Loubère. A high-order finite volume method for systems of conservation laws—multi-dimensional optimal order detection (mood). *Journal of computational Physics*, 230(10):4028–4050, 2011.

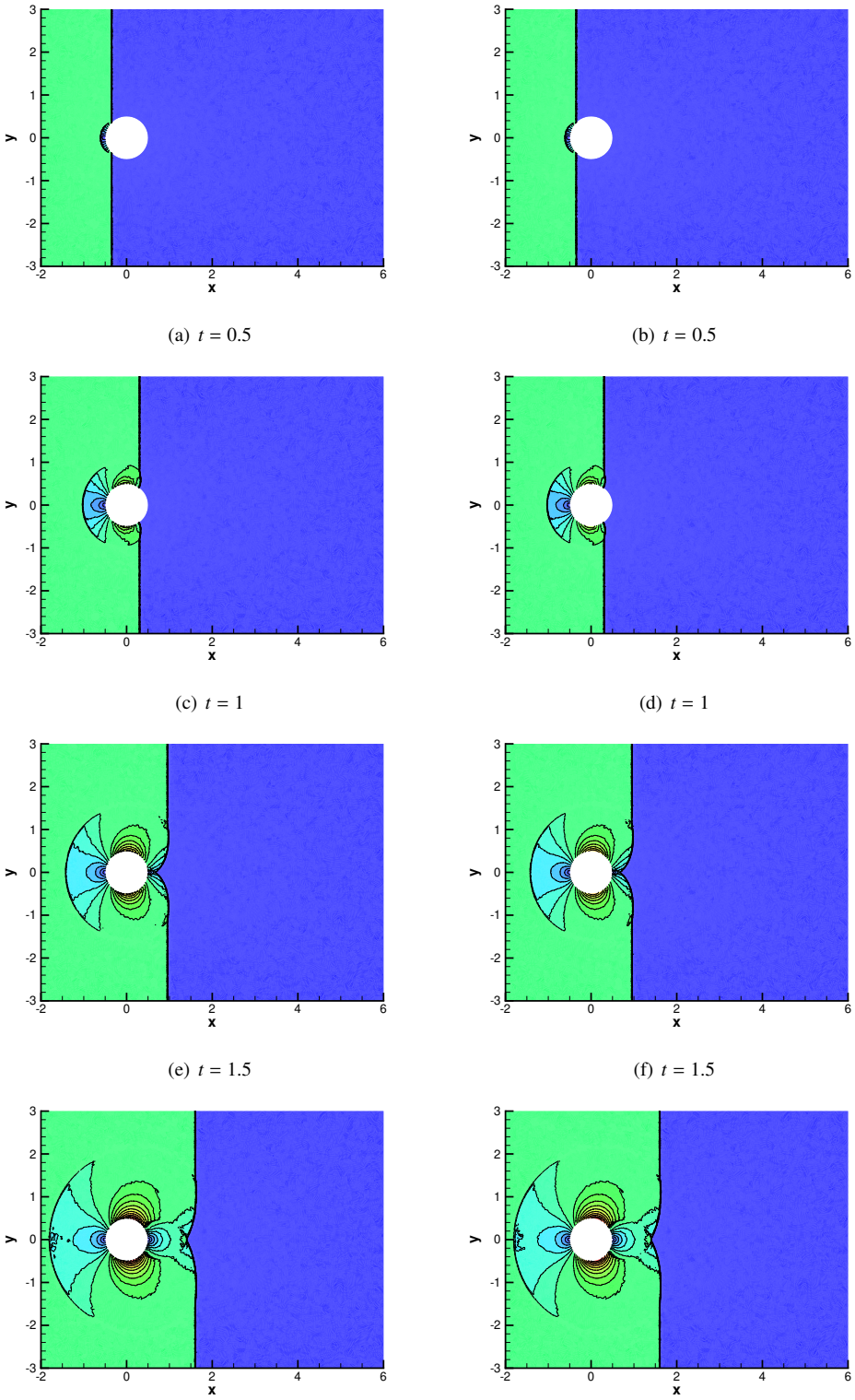

(a) $t = 0.5$ (b) $t = 0.5$

(c) $t = 1$ (d) $t = 1$

(e) $t = 1.5$ (f) $t = 1.5$

(g) $t = 2$ (h) $t = 2$

Figure 13: Shock-cylinder interaction of Section 5.3. We show the Mach number iso-contours at different time steps (simulation run with DG-$\mathbb{P}3$ on the left and DG-$\mathbb{P}3$/SBM-$\mathbb{P}3$ on the right).

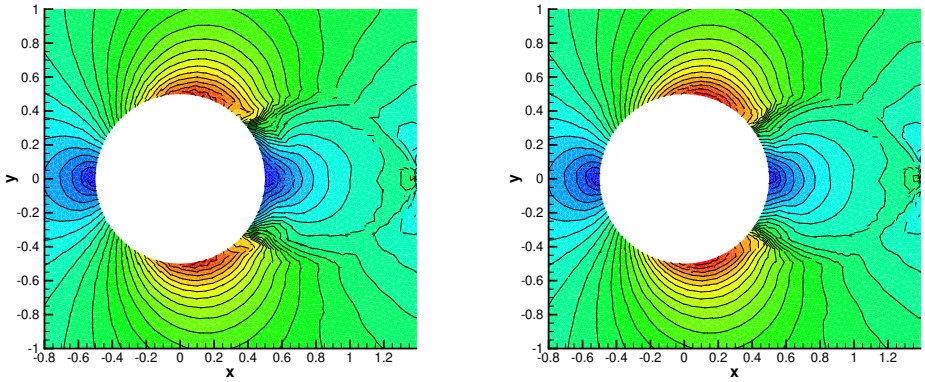

(a) DG-$\mathbb{P}1$ (b) DG-$\mathbb{P}1$/SBM-$\mathbb{P}1$

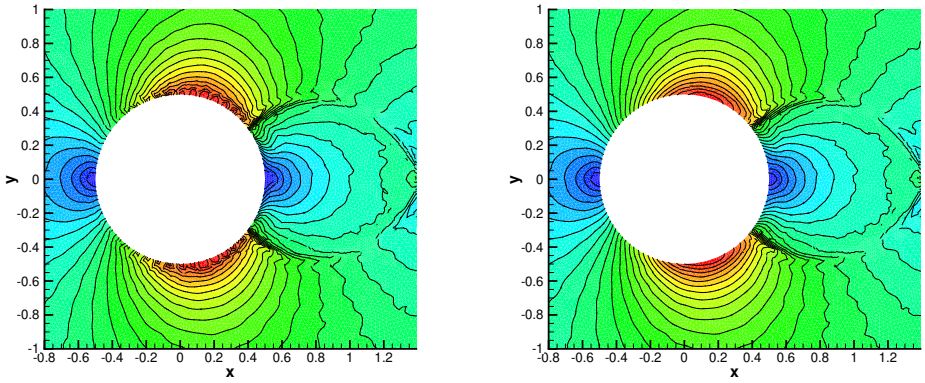

(c) DG-$\mathbb{P}2$ (d) DG-$\mathbb{P}2$/SBM-$\mathbb{P}2$

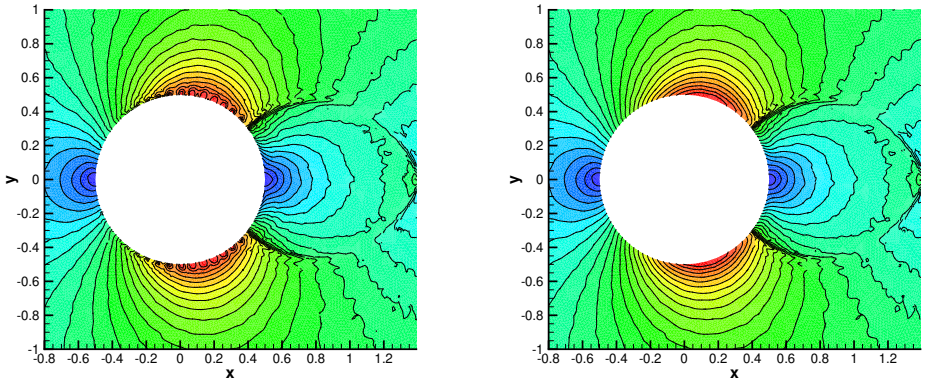

(e) DG-$\mathbb{P}3$ (f) DG-$\mathbb{P}3$/SBM-$\mathbb{P}3$

Figure 14: Shock-cylinder interaction of Section 5.3. Mach number iso-contours at the final time $t = 2$ (simulations run with several schemes).

[16] B. Cockburn and C.-W. Shu. The runge–kutta discontinuous Galerkin method for conservation laws v: multidimensional systems. *Journal of Computational Physics*, 141(2):199–224, 1998.

[17] O. Colomés, A. Main, L. Nouveau, and G. Scovazzi. A weighted shifted boundary method for free surface flow problems. *Journal of Computational Physics*, 424:109837, 2021.

[18] R. Costa, S. Clain, R. Loubère, and G. J. Machado. Very high-order accurate finite volume scheme on curved boundaries for the two-dimensional steady-state convection–diffusion equation with dirichlet condition. *Applied Mathematical Modelling*, 54:752–767, 2018.

[19] R. Costa, J. M. Nóbrega, S. Clain, G. J. Machado, and R. Loubère. Very high-order accurate finite volume scheme for the convection-diffusion equation with general boundary conditions on arbitrary curved boundaries. *International Journal for Numerical Methods in Engineering*, 117(2):188–220, 2019.

[20] M. Couplet, M. Reberol, and J.-F. Remacle. *Generation of High-Order Coarse Quad Meshes on CAD Models via Integer Linear Programming*.

[21] S. Dey, R. M. O'Bara, and M. S. Shephard. Towards curvilinear meshing in 3d: the case of quadratic simplices. *Computer-Aided Design*, 33(3):199–209, 2001.

[22] S. Diot, S. Clain, and R. Loubère. Improved detection criteria for the multi-dimensional optimal order detection (mood) on unstructured meshes with very high-order polynomials. *Computers & Fluids*, 64:43–63, 2012.

[23] S. Diot, R. Loubère, and S. Clain. The multidimensional optimal order detection method in the three-dimensional case: very high-order finite volume method for hyperbolic systems. *International Journal for Numerical Methods in Fluids*, 73(4):362–392, 2013.

[24] M. Dumbser, D. S. Balsara, E. F. Toro, and C.-D. Munz. A unified framework for the construction of one-step finite volume and discontinuous Galerkin schemes on unstructured meshes. *Journal of Computational Physics*, 227(18):8209–8253, 2008.

[25] M. Dumbser, F. Fambri, E. Gaburro, and A. Reinarz. On GLM curl cleaning for a first order reduction of the CCZ4 formulation of the einstein field equations. *Journal of Computational Physics*, 404:109088, 2020.

[26] M. Dumbser, F. Guercilena, S. Köppel, L. Rezzolla, and O. Zanotti. Conformal and covariant Z4 formulation of the einstein equations: strongly hyperbolic first-order reduction and solution with discontinuous Galerkin schemes. *Physical Review D*, 97(8):084053, 2018.

[27] M. Dumbser, I. Peshkov, E. Romenski, and O. Zanotti. High order ader schemes for a unified first order hyperbolic formulation of continuum mechanics: viscous heat-conducting fluids and elastic solids. *Journal of Computational Physics*, 314:824–862, 2016.

[28] F. Fambri, M. Dumbser, S. Köppel, L. Rezzolla, and O. Zanotti. ADER discontinuous Galerkin schemes for general-relativistic ideal magnetohydrodynamics. *Monthly Notices of the Royal Astronomical Society*, 477(4):4543–4564, 2018.

[29] F. Fambri, M. Dumbser, and O. Zanotti. Space–time adaptive ader-dg schemes for dissipative flows: Compressible navier–stokes and resistive mhd equations. *Computer Physics Communications*, 220:297–318, 2017.

[30] J. Fernández-Fidalgo, S. Clain, L. Ramírez, I. Colominas, and X. Nogueira. Very high-order method on immersed curved domains for finite difference schemes with regular cartesian grids. *Computer Methods in Applied Mechanics and Engineering*, 360:112782, 2020.

[31] M. Fortunato and P.-O. Persson. High-order unstructured curved mesh generation using the winslow equations. *Journal of Computational Physics*, 307:1–14, 2016.

[32] A.-A. Gabriel, D. Li, S. Chiocchetti, M. Tavelli, I. Peshkov, E. Romenski, and M. Dumbser. A unified first-order hyperbolic model for nonlinear dynamic rupture processes in diffuse fracture zones. *Philosophical Transactions of the Royal Society A*, 379(2196):20200130, 2021.

[33] E. Gaburro. A unified framework for the solution of hyperbolic pde systems using high order direct arbitrary-lagrangian–eulerian schemes on moving unstructured meshes with topology change. *Archives of Computational Methods in Engineering*, 28(3):1249–1321, 2021.

[34] E. Gaburro, W. Boscheri, S. Chiocchetti, C. Klingenberg, V. Springel, and M. Dumbser. High order direct Arbitrary-Lagrangian–Eulerian schemes on moving voronoi meshes with topology changes. *Journal of Computational Physics*, 407:109167, 2020.

[35] E. Gaburro and M. Dumbser. A posteriori subcell finite volume limiter for general PNPM schemes: Applications from gasdynamics to relativistic magnetohydrodynamics. *Journal of Scientific Computing*, 86(3):1–41, 2021.

[36] E. Gaburro, P. Öffner, M. Ricchiuto, and D. Torlo. High order entropy preserving ADER scheme. *arXiv preprint arXiv:2206.03889*, 2022.

[37] A. Gargallo-Peiró, X. Roca, J. Peraire, and J. Sarrate. Optimization of a regularized distortion measure to generate curved high-order unstructured tetrahedral meshes. *International Journal for Numerical Methods in Engineering*, 103(5):342–363, 2015.

[38] C. Geuzaine and J.-F. Remacle. Gmsh: A 3-d finite element mesh generator with built-in pre- and post-processing facilities. *International Journal for Numerical Methods in Engineering*, 79(11):1309–1331, 2009.

[39] S. Gottlieb, C.-W. Shu, and E. Tadmor. Strong stability-preserving high-order time discretization methods. *SIAM review*, 43(1):89–112, 2001.

[40] M. Han Veiga, P. Öffner, and D. Torlo. Dec and ader: similarities, differences and a unified framework. *Journal of Scientific Computing*, 87(1):1–35, 2021.

[41] T. Hughes, J. Cottrell, and Y. Bazilevs. Isogeometric analysis: Cad, finite elements, nurbs, exact geometry, and mesh refinement. *Computer Methods in Applied Mechanics and Engineering*, 194:33–40, 2005.

[42] F. Kemm, E. Gaburro, F. Thein, and M. Dumbser. A simple diffuse interface approach for compressible flows around moving solids of arbitrary shape based on a reduced baer–nunziato model. *Computers & fluids*, 204:104536, 2020.

[43] L. Krivodonova and M. Berger. High-order accurate implementation of solid wall boundary conditions in curved geometries. *Journal of computational physics*, 211(2):492–512, 2006.

[44] M. Lesueur, H. Rattez, and O. Colomés. μct scans permeability computation with an unfitted boundary method to improve coarsening accuracy. *Computers & Geosciences*, page 105118, 2022.

[45] K. Li, N. M. Atallah, G. A. Main, and G. Scovazzi. The shifted interface method: A flexible approach to embedded interface computations. *International Journal for Numerical Methods in Engineering*, 121(3):492–518, 2020.

[46] A. Loseille and L. Rochery. *Developments on the P^2 cavity operator and Bézier Jacobian correction using the simplex algorithm.*

[47] R. Loubere, M. Dumbser, and S. Diot. A new family of high order unstructured MOOD and ADER finite volume schemes for multidimensional systems of hyperbolic conservation laws. *Communications in Computational Physics*, 16(3):718–763, 2014.

[48] X.-J. Luo, M. S. Shephard, R. M. O'bara, R. Nastasia, and M. W. Beall. Automatic p-version mesh generation for curved domains. *Engineering with Computers*, 20(3):273–285, 2004.

[49] A. Main and G. Scovazzi. The shifted boundary method for embedded domain computations. part I: Poisson and Stokes problems. *Journal of Computational Physics*, 372:972–995, 2018.
[50] A. Main and G. Scovazzi. The shifted boundary method for embedded domain computations. part II: Linear advection–diffusion and incompressible Navier–Stokes equations. *Journal of Computational Physics*, 372:996–1026, 2018.
[51] A. Mazaheri, C.-W. Shu, and V. Perrier. Bounded and compact weighted essentially nonoscillatory limiters for discontinuous Galerkin schemes: Triangular elements. *Journal of Computational Physics*, 395:461–488, 2019.
[52] G. I. Montecinos and E. F. Toro. Reformulations for general advection–diffusion–reaction equations and locally implicit ADER schemes. *Journal of Computational Physics*, 275:415–442, 2014.
[53] D. Moxey, D. Ekelschot, Ü. Keskin, S. Sherwin, and J. Peiró. High-order curvilinear meshing using a thermo-elastic analogy. *Computer-Aided Design*, 72:130–139, 2016.
[54] L. Nouveau, M. Ricchiuto, and G. Scovazzi. High-order gradients with the shifted boundary method: An embedded enriched mixed formulation for elliptic pdes. *Journal of Computational Physics*, 398:108898, 2019.
[55] I. Peshkov, M. Dumbser, W. Boscheri, E. Romenski, S. Chiocchetti, and M. Ioriatti. Simulation of non-newtonian viscoplastic flows with a unified first order hyperbolic model and a structure-preserving semi-implicit scheme. *Computers & Fluids*, 224:104963, 2021.
[56] O. Sahni, X. Luo, K. Jansen, and M. Shephard. Curved boundary layer meshing for adaptive viscous flow simulations. *Finite Elements in Analysis and Design*, 46(1-2):132–139, 2010.
[57] T. Song, A. Main, G. Scovazzi, and M. Ricchiuto. The shifted boundary method for hyperbolic systems: Embedded domain computations of linear waves and shallow water flows. *Journal of Computational Physics*, 369:45–79, 2018.
[58] M. Tavelli and M. Dumbser. A pressure-based semi-implicit space–time discontinuous Galerkin method on staggered unstructured meshes for the solution of the compressible navier–stokes equations at all mach numbers. *Journal of Computational Physics*, 341:341–376, 2017.
[59] M. Tavelli and M. Dumbser. Arbitrary high order accurate space–time discontinuous Galerkin finite element schemes on staggered unstructured meshes for linear elasticity. *Journal of Computational Physics*, 366:386–414, 2018.
[60] V. A. Titarev and E. F. Toro. Ader: Arbitrary high order godunov approach. *Journal of Scientific Computing*, 17(1):609–618, 2002.
[61] V. A. Titarev and E. F. Toro. Ader schemes for three-dimensional non-linear hyperbolic systems. *Journal of Computational Physics*, 204(2):715–736, 2005.
[62] E. F. Toro and V. A. Titarev. Derivative riemann solvers for systems of conservation laws and ADER methods. *Journal of Computational Physics*, 212(1):150–165, 2006.
[63] T. Toulorge, C. Geuzaine, J.-F. Remacle, and J. Lambrechts. Robust untangling of curvilinear meshes. *Journal of Computational Physics*, 254:8–26, 2013.
[64] M. Turner, J. Peiró, and D. Moxey. Curvilinear mesh generation using a variational framework. *Computer-Aided Design*, 103:73–91, 2018.
[65] A. Veilleux, G. Puigt, H. Deniau, and G. Daviller. A stable spectral difference approach for computations with triangular and hybrid grids up to the 6th order of accuracy. *Journal of Computational Physics*, 449:110774, 2022.
[66] Z. Wang, K. Fidkowski, R. Abgrall, F. Bassi, D. Caraeni, A. Cary, H. Deconinck, R. Hartmann, K. Hillewaert, H. Huynh, N. Kroll, G. May, P.-O. Persson, B. van Leer, and M. Visbal. High-order cfd methods: current status and perspective. *International Journal for Numerical Methods in Fluids*, 72(8):811–845, 2013.
[67] Z. Wang and Y. Sun. Curvature-based wall boundary condition for the euler equations on unstructured grids. *AIAA journal*, 41(1), 2003.
[68] O. Zienkiewicz and P. Morice. *The finite element method in engineering*. McGraw-Hill, 1971.